NONLINEAR DYNAMICS-DRIVEN QUANTUM ANALOGUES IN CLASSICAL GRANULAR METAMATERIALS

by

KAZI TAHSIN MAHMOOD

Submitted to the Graduate School

of Wayne State University,

Detroit, Michigan

in partial fulfillment of the requirements

for the degree of

MASTER OF SCIENCE

2025

MAJOR: MECHANICAL ENGINEERING

Signature **Date**

ACKNOWLEDGEMENTS

I would like to express my sincere gratitude to the Department of Mechanical Engineering at Wayne State University in Detroit, Michigan, for providing the necessary resources and support for this study. I want to extend my appreciation to my friend and group member, **Abrar Nur-E Faiaz**, for his collaboration and assistance with various analyses throughout this research. Lastly, I would like to express my heartfelt appreciation to my esteemed supervisor, **Dr. M. Arif Hasan**, Assistant Professor in the Department of Mechanical Engineering at Wayne State University, Detroit, MI, for his guidance and supervision throughout this thesis work. Our group and I would like to thank you for the funding support from NSF Grants 2204382 and 2242925.

TABLE OF CONTENTS

LIST OF FIGURES

1. INTRODUCTION

1.1. Quantum System and Their Applications:

Quantum information science represents one of the most significant advancements in modern technology, offering unprecedented opportunities for revolutionary breakthroughs in computing, communications, and sensing applications [1-5]. This interdisciplinary field leverages the principles of quantum mechanics, exploiting phenomena such as superposition, entanglement, and quantum coherence to enhance computational capabilities and security far beyond the reach of classical systems [6-8]. Quantum technologies have demonstrated considerable promise in tackling computationally challenging problems across diverse domains, including cryptography, materials science, pharmaceutical development, and complex optimization problems.

At the heart of quantum information technology lies the quantum bit, also known as a qubit. Unlike classical bits that encode information strictly in binary states (0 or 1), qubits capitalize on the quantum mechanical principle of superposition, enabling simultaneous existence in multiple states [9]. This extraordinary capability allows quantum systems to accelerate computational tasks exponentially. Quantum algorithms, such as Shor's algorithm for integer factorization and Grover's algorithm for database searches, exemplify this superior computational power, providing significant speed-ups compared to classical algorithms [10-12]. Additionally, quantum computing promises substantial advancements in simulating quantum mechanical systems, which will significantly benefit chemical simulations, materials discovery, and drug development [13, 14].

A new and distinct quantum state that emerges from specific quantitative relationships with initial states is known as a superposition of these original states. Beyond enabling the superposition of states, the phenomenon of entanglement—where subsystems become intricately correlated—significantly amplifies the computational prowess of qubits [15, 16]. Nevertheless, these quantum states are exceptionally fragile, with environmental interactions rapidly causing decoherence and the subsequent collapse of quantum coherence. Due to this rapid loss of coherence, it remains exceedingly challenging to reliably create and maintain initial quantum superposed states for practical applications.

1.2. Granular Systems and Their Application in Quantum System:

Granular systems, consisting of discrete macroscopic particles interacting through strongly nonlinear contact forces, represent a compelling domain for exploring quantum-inspired phenomena within classical frameworks. These systems, composed of particles typically interacting via Hertzian contact mechanics, are uniquely positioned at the intersection of nonlinear dynamics and classical mechanics, exhibiting rich and complex behaviors such as solitary wave propagation, nonlinear resonances, and nonlinear normal modes [17].

Unlike traditional linear elastic media, granular systems inherently feature nonlinear interactions due to their geometry-dependent force-displacement relationships. This intrinsic nonlinearity facilitates dynamic phenomena closely analogous to quantum mechanical concepts, including the formation of stable superpositions and classical analogues of quantum entanglement [18]. Such properties make granular media especially promising as platforms for developing macroscopic quantum analogues—robust systems that can mimic quantum-like behavior at room temperature and under practical environmental conditions.

1.3. Limitations of the Quantum Mechanical System

Consequently, quantum systems used in practical quantum computing applications typically require stringent environmental conditions, such as ultra-low temperatures near absolute zero, vacuum environments, and electromagnetic shielding [19-21]. These extreme conditions significantly limit the practical implementation of quantum systems, thus hindering widespread adoption. Research efforts have successfully demonstrated quantum superposition experimentally in various microscopic systems, such as trapped ions, Bose-Einstein condensates, and atomic ensembles, achieving remarkable precision under carefully controlled laboratory conditions [22-24].

Recognizing the significant hurdles presented by quantum decoherence and the challenges faced by topological quantum computing, researchers have actively pursued alternative strategies involving macroscopic superpositions in classical systems. These macroscopic superposition states, which can be achieved at room temperature and in less stringent environments, present compelling avenues for robust quantum-like computation [25, 26]. Recent successful demonstrations of macroscopic superposition have included experiments with trapped ions, atomic ensembles, and mechanical oscillators interacting with spin qubits, opening up possibilities for exploring quantum-like phenomena on macroscopic scales [27, 28].

1.4. Motivation of the Study:

To overcome these limitations, researchers have explored alternative approaches, such as topological quantum computing (TPC), where the quantum information is encoded using topological properties on a macroscopic scale. TPC leverages non-Abelian statistics and topological states of matter to create more robust qubits that are inherently resistant to decoherence

[29, 30]. However, recent challenges highlighted by researchers, including a notable critique by Frolov in Nature, have cast doubt on the feasibility of reliably generating and detecting topological qubits, such as Majorana particles [31]. The certainty and advancement of TPC techniques has been limited by this argument, which has led to a wider hunt for stronger and more practical substitutes.

The establishment of acoustic analogues of quantum phenomena has provided additional perspectives for quantum information science and quantum mechanics applications. Notably, linear elastic systems have been shown, to produce coherent superpositions of classical harmonic waves analogous to spin states in quantum mechanics [32]. However, genuine quantum-like phenomena in mechanical systems necessitate inherent nonlinearity. For instance, generating mechanical non-Gaussian states with unfavorable Wigner functions exemplifies actual quantum-like behavior in classical systems [33-36]. Approaches involving dissipation, quantum tunneling in double-well optomechanical potentials, periodic qubit flipping, quantum interference effects, optical field conditional measurements, and modulated photon-hopping interactions between optomechanical cavities have successfully produced macroscopic non-Gaussian superposition states [37-45]. These approaches rely fundamentally on nonlinear interactions between optical and mechanical degrees of freedom. Recent studies have demonstrated the experimental generation of macroscopic superposition states using Kerr-type nonlinearities, where external driving fields are manipulated to induce state transitions [46].

In contrast, limited work has been conducted on utilizing nonlinearity within classical elastic systems for creating stable macroscopic superpositions of states. Nonlinear granular media represents a promising platform for this endeavor. Granular media consist of discrete, macroscopic particles interacting through strongly nonlinear Hertzian contact mechanics, facilitating complex phenomena such as solitary wave propagation and nonlinear normal modes [47]. These properties enable granular systems to exhibit quantum-like behaviors, including the remarkably coherent superposition of elastic states and classical entanglement.

Recent experimental and theoretical advancements, including extensive research conducted by the author, have demonstrated the capability of nonlinear granular chains to sustain coherent elastic superposition states. These elastic states, inherently robust and stable under ambient conditions, serve as a foundation for developing "elastic bits," analogues to quantum bits. Elastic bits exploit the intrinsic nonlinearities of granular particle interactions, maintaining coherent superpositions and classical entanglement without succumbing to quantum decoherence.

By harmonically driving a nonlinear granular system composed of two spherical granules, we experimentally demonstrate that nonlinear normal modes can be expressed in terms of a linear normal mode orthonormal basis with time-dependent amplitudes [48]. An elastic bit in a nonlinear classical system can create a superposition of states that is stable at ambient temperature and decoherence-free. Furthermore, since it represents an actual amplitude rather than a probability amplitude, it can be measured directly in the absence of wave function collapse. These characteristics make it possible for an elastic bit to be realized experimentally, providing a revolutionary new way to accomplish some of the objectives of quantum information technology utilizing materials-based quantum analogues. The present study’s objective is to experimentally demonstrate the possibility of preparing acoustic analogues of superposition states in a nonlinear acoustic granular medium and manipulating the superposition of Bloch states. More specifically, by harmonically driving a nonlinear system composed of two spherical granules, we experimentally demonstrate that the nonlinear normal modes can be expressed on a linear normal mode orthonormal basis with time-dependent amplitudes. These amplitudes form the components of a state vector that spans a two-dimensional (2D) Hilbert space parametrically with time. Thus, they serve as analogues of the qubit-like time-dependent coherent superpositions of states. In addition, we experimentally demonstrate that the frequency and amplitude of the external drivers applied to the nonlinear system are essential factors in navigating the elastic Bloch sphere. Most profoundly, since the system under consideration is nonlinear, we experimentally show that time permits the parametric exploration of the superposition of Bloch states.

Ultimately, this research seeks to position granular networks as robust, practical, and widely accessible analogues to quantum computing systems. The investigation aims to foster significant advancements in classical computing technologies by bridging quantum-inspired capabilities with practical, real-world robustness. Through the development and validation of elastic bits, this dissertation contributes toward a new paradigm in information science, combining the profound computational advantages of quantum mechanics with the inherent practicality and robustness of classical nonlinear systems, thus opening new frontiers in computing and technological innovation.

2. BACKGROUND AND TUNABLE CHARACTERISTICS OF GRANULAR NETWORK THROUGH THEORETICAL AND MATHEMATICAL MODELLING

Understanding the unique dynamical properties of granular systems lays the foundation for exploiting their potential in simulating quantum-like behaviors. These systems, composed of discrete elastic particles, demonstrate strongly nonlinear interactions, especially when confined to fixed geometries. We begin by establishing the foundational definitions and configurations before delving into governing mathematics and its relevance in emerging quantum-analog applications.

2.1. Specification of Granular Network:

To study wave propagation and nonlinear phenomena in granular media, we first define a structured granular network, commonly referred to as a granular crystal. These ordered assemblies of elastic particles (typically spherical) interact through direct mechanical contact, allowing transmission of force through strongly nonlinear Hertzian contact laws. Their spatial arrangement, whether one-dimensional chains or higher-dimensional lattices, sets the stage for complex dynamics that are not present in traditional linear systems.

This structural specificity is what enables granular crystals to support phenomena such as solitary waves and nonlinear normal modes. The elastic nature of the contact and the absence of tensile strength in the interaction give rise to asymmetric, non-synchronous oscillations across the lattice. The key features of the granular networks:

- **Elastic Particles in Contact:** Granular crystals typically consist of elastic spheres arranged systematically in linear chains or two-dimensional and three-dimensional lattices. These arrangements provide direct mechanical pathways for the transmission of force and the propagation of waves.

- **Asymmetric and Non-synchronous Oscillations:** Unlike linear elastic systems, granular crystals demonstrate highly asymmetric oscillations, where individual granules oscillate independently rather than synchronously. This behavior arises from the nonlinear interaction forces, resulting in complex wave propagation and localized energy transfer within the network.
- **Fermi-Pasta-Ulam (FPU) Lattice Analogy:** Granular crystals exhibit similarities with Fermi-Pasta-Ulam lattices, renowned for their intricate nonlinear dynamics, including energy localization, wave breaking, and the formation of solitary waves. These analogies allow researchers to utilize established knowledge from nonlinear physics to understand better and predict granular behavior.
- **Highly Tunable Dynamics:** Granular crystals offer highly tunable mechanical properties through the manipulation of several parameters, including granule size, material composition, contact geometry, applied static pre-compression, and environmental conditions. This tunability enables precise control over wave dynamics, facilitating targeted applications like energy absorption, signal processing, and novel metamaterial design.

2.2. Typical configurations of granular networks include:

Building upon the definition of granular crystals, various configurations have been developed to tailor wave dynamics. Each configuration introduces a distinct mechanical response:

- **Homogeneous System:** In homogeneous granular systems, identical granules are uniformly arranged, resulting in consistent and predictable dynamic behavior. Such uniformity allows for simple analytical modeling and facilitates investigations into fundamental wave propagation phenomena and energy transport mechanisms.

- **Diatomic or Dimer Chain:** Diatomic chains consist of alternating sequences of large and small granules, introducing periodic variation in mass and stiffness throughout the network. This periodicity creates band-gap effects, unique dispersion characteristics, and controlled wave transmission behaviors, which help filter frequencies, isolate vibrations, and design waveguides.
- **Tapered Chain:** Tapered granular chains feature a gradual change in granule size along their length. This structural gradient has a significant impact on local stiffness and mass distribution, enabling precise wave manipulation, such as energy focusing, shock wave attenuation, and tailored stress wave profiles. These chains are particularly beneficial in applications that require impact mitigation and energy localization.
- **Tapered Dimer Chain:** Tapered dimer chains combine the structural gradient characteristics of tapered chains with the periodic mass variations of diatomic chains. This complex configuration enhances the ability to control wave propagation, achieve efficient energy trapping, and facilitate targeted wave attenuation. These structures possess advanced capabilities in applications that require high levels of vibration isolation and precise energy management.

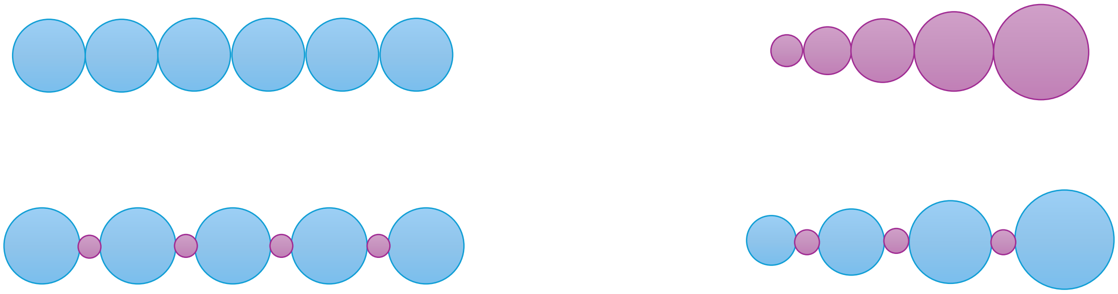

Figure 1: Typical configurations of granular networks: (Top-left) Homogeneous System consisting of identical granules uniformly arranged; (Top-right) Tapered Chain with granules gradually increasing in size; (Bottom-left) Diatomic or Dimer Chain featuring altering large and small granules; (Bottom-right) Tapered Dimer Chain combining periodic mass variations with a gradual structural gradient. These configurations illustrate the diversity in structural designs, each enabling distinct and tunable wave propagation and energy management characteristics in granular networks.

2.3. Mathematical Background of Granular Systems:

Having outlined the structural possibilities, we now transition into a mathematical formalism that governs granular dynamics. The Hertzian contact law — a nonlinear force-displacement relationship — serves as the core mechanism dictating how energy propagates within these systems. Using this foundation, we develop discrete models of motion that capture both linear and nonlinear responses under varying precompression and external excitation.

2.3.1. Discrete Modeling and Contact Laws:

To mathematically describe interactions in granular chains, we employ a discrete mass-spring model, where each granule is represented as a point mass connected by nonlinear springs.

A typical granular system consists of spherical particles arranged in a one-dimensional (1D) chain, two-dimensional (2D) lattice, or three-dimensional (3D) array. In most analytical and experimental studies, the one-dimensional chain of granules is the canonical model due to its tractability and its ability to reveal the essential nonlinear characteristics of the system.

Let us consider a one-dimensional granular chain composed of N spherical particles, each of mass m and radius R. These granules are aligned such that each particle is in mechanical contact only with its nearest neighbors. For simplicity, and unless stated otherwise, we consider identical spherical granules of mass m and radius R. The particles are either under no external compression (zero precompression) or under a uniform static compressive force F_0 leading to a finite precompression at equilibrium. The granules are constrained to move only along the longitudinal axis (say, the x-axis), and their displacements from equilibrium are denoted as $u_i(t)$, where $i = 1,2,\dots,N$, The boundary conditions can be fixed, free, or driven (e.g., by actuators or shakers), depending on the specific setup.

Figure 2: Hertzian Contacting Granules. A series of Granules are connected in a series and the repelling force (F) varies nonlinearity with deformation δ.

The Hertzian contact law describes the elastic interaction force between two curved bodies—typically spheres—when they are pressed together. First formulated by Heinrich Hertz in 1882, this theory forms the foundational basis for modeling contact forces in granular systems. In the context of granular chains composed of spherical granules, the Hertzian law quantifies the growth of the contact force as the particles are compressed against one another.

2.3.2. Geometric Relation:

The contact geometry between two granules significantly contributes to the nonlinear behavior. Assuming spherical symmetry and small deformation, the effective contact radius and Young's modulus enable us to derive expressions for the contact area, pressure distribution, and total force, culminating in the Hertzian law. This geometric relation is essential for accurately modeling the system's response under compression and plays a critical role in later perturbation-based expansions of the equations of motion.

When two spheres are pressed together by force, their point of contact flattens slightly, creating a circular contact area. The deformation or indentation at the contact, δ, is defined as the overlap distance from the undeformed positions. There are some assumptions for the contacting granules are considered:

- The contact is at a point under no load condition
- The contact surface is elliptical upon the application of loads.
- Small deformation (small contact area) i.e. $\delta \ll R$
- Sufficiently stiff bead material (linear elasticity)
- Speed of wave in chain << speed of sound in bead material (quasistatic)
- System of nonlinear springs and point masses

The effective radius R^* of the two contacting spheres is defined by:

$$\frac{1}{R^*} = \frac{1}{R_1} + \frac{1}{R_2} \tag{1}$$

Where, $R^* = \frac{R_1 R_2}{R_1 + R_2}$ is the effective radius. R_1 and R_2 are the contacting granule's radius. And the effective elastic modulus of the granules can be written as,

$$\frac{1}{E^*} = \frac{1-\nu_1^2}{E_1} + \frac{1-\nu_2^2}{E_2} \tag{2}$$

Here E_1 and E_2 are the Young's modulus and the ν_1 and ν_2 are the poison's ratio for the contacting granules. The effective Young's modulus and effective radius can be written as for a uniform material is,

$$E^* = \frac{E}{2(1-\nu^2)}, \quad R^* = \frac{R}{2} \tag{3}$$

Figure 3: Hertzian contact and deformation of the granules. It represents the deformation of the granules at the contact point.

The geometry of deformation at the contact region can be mathematically described through the relationship between the indentation δ, the radial distance from the center of contact, and the effective radius R^*, which takes the form: $\delta = \frac{r^2}{2R^*}$. This relationship captures the parabolic nature of the deformation profile around the contact point.

Where, r is the radial distance from the center of the contact. The geometry of the deformation of the contact can be written as,

$$a^2 = R^*\delta \Rightarrow a = \sqrt{R^*\delta} \tag{4}$$

We have assumed that the contact of the elastic materials is isotropic. The normal stress distribution under spherical contact is given by Hertzian theory, which yields the following relationships between load and deformation. The contact pressure distribution $p(r)$ across a circular contact area of a radius a is given by,

$$p(r) = p_0\sqrt{\left(1 - \frac{r^2}{a^2}\right)}, \qquad r \leq a \tag{5}$$

Here, p_0 is the maximum contact pressure at the center. The total load F acting on the spheres is the integral of pressure over the contact area:

$$F = \int_0^{2\pi}\int_0^a p(r)rdrd\theta = \int_0^{2\pi}\int_0^a p_0\sqrt{\left(1 - \frac{r^2}{a^2}\right)}rdrd\theta$$

$$F = 2\pi p_0 \int_0^a r\sqrt{1 - \frac{r^2}{a^2}}dr \tag{6}$$

Solving this equation, we get the total load as:

$$F = \frac{2\pi p_0 a^2}{3} \tag{7}$$

This nonlinear force-displacement relationship, known as the Hertzian contact law, is essential for accurately describing the behavior of granular systems. Such systems governed by strongly nonlinear interactions exhibit complex dynamic behaviors, including the formation of solitary waves, nonlinear normal modes, and distinct propagation characteristics. These phenomena significantly influence the acoustic response, dynamic load transmission, and energy dissipation properties in granular media, making them particularly interesting for advanced engineering applications such as impact mitigation, acoustic filtering, and granular metamaterials.

2.3.3. Relative Displacement and Overlap:

We next quantify the dynamic overlap between neighboring particles as a function of their displacements from equilibrium. This enables the transformation of geometric deformations into relative coordinates, which are suitable for modeling forces and motions within the chain. These relationships become especially important when extending the analysis to include higher-order nonlinear effects and interactions involving multiple characteristic frequencies.

The foundational principle governing granular dynamics is the Hertzian contact law, describing the force between two spherical granules compressed by a displacement δ:

$$F = k_{NL}\delta^{\frac{3}{2}} \tag{8}$$

where k_{NL} is the contact stiffness coefficient, dependent on the geometric and elastic properties of the granules and δ is the overlap or relative displacement between particles. The Hertzian relationship is inherently nonlinear, demonstrated by the exponent $3/2$, and is unilateral, indicating zero force under tensile conditions $(\delta < 0)$. This constraint ensures granules cannot sustain tension, distinguishing granular materials from traditional elastic media and giving rise to their strongly nonlinear, non-smooth characteristics.

$$k_{NL} = \frac{4}{3}E^{*}\sqrt{R^{*}} = \frac{E\sqrt{2R}}{3(1-\nu^{2})} \tag{9}$$

In a linear chain of granules, the overlap between adjacent particles i and $i+1$ can be defined as:

$$\delta_i = u_i - u_{i+1} + \delta_0 \tag{10}$$

Where u_i and u_{i+1} are the displacement of particles i and $i+1$, respectively, and δ_0 represents the initial static precompression. When the chain is initially uncompressed, δ_0. Thus, the Hertzian contact force between particles i and $i+1$ becomes:

$$F_i = k_{NL}[\delta_i]_{+}^{\frac{3}{2}} = k_{NL}[u_i - u_{i+1} + \delta_0]^{3/2} \tag{11}$$

The operator $[x]_{+} \equiv \max(x, 0)$ ensures that the contact force only exists when the two particles are in contact (i.e. when the argument is positive).

2.3.4. Equation of Motion:

By applying Newton's second law to each granule, we obtain a set of coupled nonlinear differential equations that govern the temporal evolution of the system. These equations encompass both inertial terms and nonlinear elastic restoring forces, with damping optionally included to account for energy losses. This formulation sets the stage for exploring reduced-order models and perturbation approaches that capture essential behaviors, particularly under harmonic excitation. For the i-th granule, this equation is:

$$m\ddot{u}_i = k_{NL}(u_{i-1} - u_i + \delta_0)_{+}^{\frac{3}{2}} - k_{NL}(u_i - u_{i+1} + \delta_0)_{+}^{\frac{3}{2}} - \eta\dot{u}_i \tag{12}$$

Here, m is the mass of each particle, and the subscripts represent the overlaps between adjacent granules. The equation clearly illustrates that each particle's motion depends on the relative displacement (compression) with its neighboring particles.

2.4. Two-Mass Granular Network:

With the foundational models established, we simplify the system to a two-mass granular network to examine specific nonlinear behaviors in greater detail. This minimal model retains the core Hertzian nonlinearity, allowing for a tractable analysis of wave dynamics, energy transfer, and coherent state formation.

Here, we consider two spherical granules, each with a mass $m = \frac{4}{3}\pi\rho R^3$, where R is the radius, and ρ is the density of the granules and u_1 and u_2 are the displacements of the granules from the equilibrium. The system is subjected to external harmonic excitations with magnitudes F_1 and F_2 at a driving frequency ω_D. The static precompression applied to the granules is denoted by δ_0, and the nonlinear stiffness between the granules, arising from Hertzian contact, is given by $k_{NL} = \frac{E\sqrt{2R}}{3(1-\upsilon^2)}$, where E is the Young's modulus and υ is the Poisson's ratio of the granules. The damping coefficient η models the dissipation in the system [49]. Mathematically, such a nonlinear system can be modeled by the following equations of motion for the displacements u_1 and u_2 [47]:

$$m\ddot{u}_1 = k_{NL}\left[F_1 e^{i\omega_D t} - u_1 + \delta_0\right]_+^{\frac{3}{2}} - k_{NL}[u_1 - u_2 + \delta_0]_+^{\frac{3}{2}} - \eta\dot{u}_1$$

$$m\ddot{u}_2 = k_{NL}[u_1 - u_2 + \delta_0]_+^{\frac{3}{2}} - k_{NL}\left[u_2 - F_2 e^{i\omega_D t} + \delta_0\right]_+^{\frac{3}{2}} - \eta\dot{u}_2 \tag{13}$$

2.4.1. Harmonic Responses of Granules Across Multiple Orders.

Focusing on harmonic excitation, we now expand the system's response using a Taylor series to reveal contributions from multiple harmonic orders. By applying perturbation techniques, we express the displacement field as a power series in a small parameter ϵ capturing zeroth-order (linear), first-order (primary nonlinear), and second-order (higher harmonic) responses. We are investigating a granular system composed of two granules. Considering the one-dimensional motion of the granules, the general mathematical formulation of this two-mass nonlinear granular system is given by Eq. (13). We expand Eq. (13) by applying a power expansion using the Taylor series, yielding the following expression:

$$m\ddot{u}_1 = k_{NL}[F_1 e^{i\omega_D t} - u_1 + \delta_0]_+^{\frac{3}{2}} - k_{NL}[u_1 - u_2 + \delta_0]_+^{\frac{3}{2}} - \eta\dot{u}_1$$

$$\Rightarrow m\ddot{u}_1 = k_{NL}\delta_0^{\frac{3}{2}}\left[1 + \frac{F_1 e^{i\omega_D t} - u_1}{\delta_0}\right]_+^{\frac{3}{2}} - k_{NL}\delta_0^{\frac{3}{2}}\left(1 + \frac{u_1 - u_2}{\delta_0}\right)_+^{\frac{3}{2}} - \eta\dot{u}_1$$

$$\Rightarrow m\ddot{u}_1 = k_{NL}\delta_0^{\frac{3}{2}}\left[1 + \frac{3}{2}\left(\frac{F_1 e^{i\omega_D t} - u_1}{\delta_0}\right) - \frac{3}{8}\left(\frac{F_1 e^{i\omega_D t} - u_1}{\delta_0}\right)^2 - \frac{3}{48}\left(\frac{F_1 e^{i\omega_D t} - u_1}{\delta_0}\right)^3 + \cdots\right]$$

$$- k_{NL}\delta_0^{\frac{3}{2}}\left[1 + \frac{3}{2}\left(\frac{u_1 - u_2}{\delta_0}\right) - \frac{3}{8}\left(\frac{u_1 - u_2}{\delta_0}\right)^2 - \frac{3}{48}\left(\frac{u_1 - u_2}{\delta_0}\right)^3 + \cdots\right] - \eta\dot{u}_1 \qquad (14)$$

$$\Rightarrow m\ddot{u}_1 = \left[\frac{3}{2}k_{NL}\delta_0^{\frac{1}{2}}\left(F_1e^{i\omega_D t}-u_1\right) - \frac{3}{8}k_{NL}\delta_0^{-\frac{1}{2}}\left(F_1e^{i\omega_D t}-u_1\right)^2\right.$$

$$\left. - \frac{3}{48}k_{NL}\delta_0^{-\frac{3}{2}}\left(F_1e^{i\omega_D t}-u_1\right)^3 + \cdots\right]$$

$$- \left[\frac{3}{2}k_{NL}\delta_0^{\frac{1}{2}}(u_1-u_2) - \frac{3}{8}k_{NL}\delta_0^{-\frac{1}{2}}(u_1-u_2)^2\right.$$

$$\left. - \frac{3}{48}k_{NL}\delta_0^{-\frac{3}{2}}(u_1-u_2)^3 + \cdots\right] \; - \eta\dot{u}_1$$

$$m\ddot{u}_2 = -k_{NL}\left[u_2 - F_2e^{i\omega_D t} + \delta_0\right]^{\frac{3}{2}} + k_{NL}\left[u_1 - u_2 + \delta_0\right]^{\frac{3}{2}} - \eta\dot{u}_2$$

$$\Longrightarrow m\ddot{u}_2 = -k_{NL}\delta_0^{\frac{3}{2}}\left[1 + \frac{u_2 - F_2e^{i\omega_D t}}{\delta_0}\right]^{\frac{3}{2}} + k_{NL}\delta_0^{\frac{3}{2}}\left(1 + \frac{u_1-u_2}{\delta_0}\right)^{\frac{3}{2}} - \eta\dot{u}_2$$

$$\Rightarrow m\ddot{u}_2 = -k_{NL}\delta_0^{\frac{3}{2}}\left[1 + \frac{3}{2}\left(\frac{u_2 - F_2e^{i\omega_D t}}{\delta_0}\right) - \frac{3}{8}\left(\frac{u_2 - F_2e^{i\omega_D t}}{\delta_0}\right)^2\right.$$

$$\left. - \frac{3}{48}\left(\frac{u_2 - F_2e^{i\omega_D t}}{\delta_0}\right)^3 + \cdots\right]$$

$$+ k_{NL}\delta_0^{\frac{3}{2}}\left[1 + \frac{3}{2}\left(\frac{u_1-u_2}{\delta_0}\right) - \frac{3}{8}\left(\frac{u_1-u_2}{\delta_0}\right)^2 - \frac{3}{48}\left(\frac{u_1-u_2}{\delta_0}\right)^3\right.$$

$$\left. + \cdots\right] \; - \eta\dot{u}_2$$

$$\Rightarrow m\ddot{u}_2 = -\left[\frac{3}{2}k_{NL}\delta_0^{\frac{1}{2}}\left(u_2 - F_2e^{i\omega_D t}\right) - \frac{3}{8}k_{NL}\delta_0^{-\frac{1}{2}}\left(u_2 - F_2e^{i\omega_D t}\right)^2 - \frac{3}{48}k_{NL}\delta_0^{-\frac{3}{2}}\left(u_2 - F_2e^{i\omega_D t}\right)^3 + \cdots\right] + \left[\frac{3}{2}k_{NL}\delta_0^{\frac{1}{2}}(u_1 - u_2) - \frac{3}{8}k_{NL}\delta_0^{-\frac{1}{2}}(u_1 - u_2)^2 - \frac{3}{48}k_{NL}\delta_0^{-\frac{3}{2}}(u_1 - u_2)^3 + \cdots\right] - \eta\dot{u}_2$$

By assuming $k_1 = \frac{3}{2}k_{NL}\delta_0^{\frac{1}{2}}$, $k_2 = -\frac{3}{8}k_{NL}\delta_0^{-\frac{1}{2}}$ and $k_3 = -\frac{3}{48}k_{NL}\delta_0^{-\frac{3}{2}}$ leads to Eq. . We assume the solution of the displacement field of the granules as $u_1 = u_{1,0} + \epsilon u_{1,1} + \epsilon^2 u_{1,2}$ and $u_2 = u_{2,0} + \epsilon u_{2,1} + \epsilon^2 u_{2,2}$. To carry out the asymptotic method, we introduce a small dimensionless term ϵ.

Granule 1	$$\begin{aligned} & m(\ddot{u}_{1,0} + \epsilon\ddot{u}_{1,1} + \epsilon^2\ddot{u}_{1,2}) \\ & \quad = k_1[(F_1e^{i\omega_D t} - u_{1,0}) - (u_{1,0} - u_{2,0})] \\ & \quad + \epsilon k_1[(-u_{1,1}) - (u_{1,1} - u_{2,1})] \\ & \quad + \epsilon^2 k_1[(-u_{1,2}) - (u_{1,2} - u_{2,2})] \\ & \quad + \epsilon k_2 [(F_1e^{i\omega_D t} - u_{1,0})^2 \\ & \quad + \epsilon(-2F_1e^{i\omega_D t}u_{1,1} + 2u_{1,0}u_{1,1}) - (u_{1,0} - u_{2,0})^2 \\ & \quad - \epsilon^2(2u_{1,0}u_{1,1} - 2u_{1,1}u_{2,0} - 2u_{1,0}u_{2,1} + 2u_{2,0}u_{2,1})] \\ & \quad + \epsilon^2 k_3 [(F_1e^{i\omega_D t} - u_{1,0})^3 - (u_{1,0} - u_{2,0})^3] \\ & \quad - \eta(\dot{u}_{1,0} + \epsilon\dot{u}_{1,1} + \epsilon^2\dot{u}_{1,2}) \end{aligned}$$	(15)
Granule 2	$$\begin{aligned} & m(\ddot{u}_{2,0} + \epsilon\ddot{u}_{2,1} + \epsilon^2\ddot{u}_{2,2}) \\ & \quad = k_1[(u_{1,0} - u_{2,0}) - (u_{2,0} - F_2e^{i\omega_D t})] \\ & \quad + \epsilon k_1[(u_{1,1} - u_{2,1}) - (u_{2,1})] \\ & \quad + \epsilon^2 k_1[(u_{1,2} - u_{2,2}) - (u_{1,2})] \\ & \quad + \epsilon k_2 [-(u_{2,0} - F_2e^{i\omega_D t})^2 \\ & \quad + \epsilon(2F_2e^{i\omega_D t}u_{2,1} - 2u_{2,0}u_{2,1}) + (u_{1,0} - u_{2,0})^2 \\ & \quad + \epsilon^2(2u_{1,0}u_{1,1} - 2u_{1,1}u_{2,0} - 2u_{1,0}u_{2,1} + 2u_{2,0}u_{2,1})] \\ & \quad + \epsilon^2 k_3 [(u_{1,0} - u_{2,0}) - (u_{2,0} - F_2e^{i\omega_D t})^3] \\ & \quad - \eta(\dot{u}_{2,0} + \epsilon\dot{u}_{2,1} + \epsilon^2\dot{u}_{1,2}) \end{aligned}$$	

Given the nonlinear nature of the system, we employ a regular perturbation technique to obtain approximate solutions. Introducing a small dimensionless parameter ϵ (with $\epsilon \ll 1$), we rewrite Eq. as follows:

$$
\begin{aligned}
m\ddot{u}_1 = {} & \left[k_1\left(F_1e^{i\omega_D t}-u_1\right)+\epsilon k_2\left(F_1e^{i\omega_D t}-u_1\right)^2+\epsilon k_3\left(F_1e^{i\omega_D t}-u_1\right)^3+\cdots\right] \\
& -\left[k_1(u_1-u_2)+\epsilon k_2(u_1-u_2)^2+\epsilon k_3(u_1-u_2)^3+\cdots\right] \\
& -\epsilon\eta\dot{u}_1
\end{aligned}
$$

$$
\begin{aligned}
m\ddot{u}_2 = {} & -\left[k_1\left(u_2-F_2e^{i\omega_D t}\right)+\epsilon k_2\left(u_2-F_2e^{i\omega_D t}\right)^2+\epsilon k_3\left(u_2-F_2e^{i\omega_D t}\right)^3\right. \\
& \left.+\cdots\right]+\left[k_1(u_1-u_2)+\epsilon k_2(u_1-u_2)^2+\epsilon k_3(u_1-u_2)^3+\cdots\right] \\
& -\epsilon\eta\dot{u}_2
\end{aligned}
\qquad (16)
$$

such that the solutions of the displacements can be assumed as

$$u_1 = u_{1,0}+\epsilon u_{1,1}+\epsilon^2 u_{1,2}+\cdots$$

$$u_2 = u_{2,0}+\epsilon u_{2,1}+\epsilon^2 u_{2,2}+\cdots$$

Since the damping (η) of the system is assumed to be small, we have also introduced ϵ in the damping term as well in Eq. (16). Here, $u_{1,n-1}, u_{2,n-1}; n = 1,2,3, \ldots$ represents the different orders of the displacements due to the presence of different orders of stiffness, i.e., k_1, k_2 and k_3. Substituting these expansions into Eq. (16) and equating terms of equal powers of ϵ, we derive a hierarchy of equations for each order:

$$\epsilon^0: \qquad m\ddot{u}_{1,0} = k_1\left[\left(F_1e^{i\omega_D t}-u_{1,0}\right)-\left(u_{1,0}-u_{2,0}\right)\right]-\eta\dot{u}_{1,0}$$

$$m\ddot{u}_{2,0} = k_1\left[\left(u_{1,0}-u_{2,0}\right)-\left(u_{2,0}-F_2e^{i\omega_D t}\right)\right]-\eta\dot{u}_{2,0}$$

$$\epsilon^1: \quad m\ddot{u}_{1,1} = k_1\left[\left(-u_{1,1}\right) - \left(u_{1,1} - u_{2,1}\right)\right] + k_2\left[\left(F_1 e^{i\omega_D t} - u_{1,0}\right)^2 - \left(u_{1,0} - u_{2,0}\right)^2\right] - \eta\dot{u}_{1,1}$$

$$m\ddot{u}_{2,1} = k_1\left[\left(u_{1,1} - u_{2,1}\right) - \left(u_{2,1}\right)\right] + k_2\left[\left(u_{1,0} - u_{2,0}\right)^2 - \left(u_{2,0} - F_2 e^{i\omega_D t}\right)^2\right] - \eta\dot{u}_{2,1}$$

$$\epsilon^2: \quad m\ddot{u}_{1,2} = k_1\left[\left(-u_{1,2}\right) - \left(u_{1,2} - u_{2,2}\right)\right] + k_2\left(-2F_1 e^{i\omega_D t}u_{1,1} + 2u_{1,0}u_{1,1}\right) - k_2\left(2u_{1,0}u_{1,1} - 2u_{1,1}u_{2,0} - 2u_{1,0}u_{2,1} + 2u_{2,0}u_{2,1}\right) + k_3\left[\left(F_1 e^{i\omega_D t} - u_{1,0}\right)^3 - \left(u_{1,0} - u_{2,0}\right)^3\right] - \eta\dot{u}_{1,2}$$

$$m\ddot{u}_{2,2} = k_1\left[\left(u_{1,2} - u_{2,2}\right) - \left(u_{2,2}\right)\right] + k_2\left(2F_2 e^{i\omega_D t}u_{2,1} - 2u_{2,0}u_{2,1}\right) + k_2\left(2u_{1,0}u_{1,1} - 2u_{1,1}u_{2,0} - 2u_{1,0}u_{2,1} + 2u_{2,0}u_{2,1}\right) + k_3\left[\left(u_{1,0} - u_{2,0}\right)^3 - \left(u_{2,0} - F_2 e^{i\omega_D t}\right)^3\right] - \eta\dot{u}_{2,2} \qquad (17)$$

To solve Eq. (17), we assume the solutions of the form $u_{1,n-1} = nA_{1,n-1}e^{ni\omega_D t}$ and $u_{2,n-1} = nA_{2,n-1}e^{ni\omega_D t}$. So,

$u_{1,0} = A_{1,0}e^{i\omega_D t}$	$u_{2,0} = A_{2,0}e^{i\omega_D t}$
$\dot{u}_{1,0} = i\omega_D A_{1,0}e^{i\omega_D t}$	$\dot{u}_{2,0} = i\omega_D A_{2,0}e^{i\omega_D t}$
$\ddot{u}_{1,0} = -\omega_D^2 A_{1,0}e^{i\omega_D t}$	$\ddot{u}_{2,0} = -\omega_D^2 A_{2,0}e^{i\omega_D t}$
$u_{1,1} = 2A_{1,1}e^{2i\omega_D t}$	$u_{2,1} = 2A_{2,1}e^{2i\omega_D t}$
$\dot{u}_{1,1} = 4i\omega_D A_{1,1}e^{2i\omega_D t}$	$\dot{u}_{2,1} = 4i\omega_D A_{2,1}e^{2i\omega_D t}$

$\ddot{u}_{1,1} = -8\omega_D^2 A_{1,1} e^{2i\omega_D t}$	$\ddot{u}_{2,1} = -8\omega_D^2 A_{2,1} e^{2i\omega_D t}$
$u_{1,2} = 3A_{1,2} e^{3i\omega_D t}$ $\dot{u}_{1,2} = 9i\omega_D A_{1,2} e^{3i\omega_D t}$ $\ddot{u}_{1,2} = -27\omega_D^2 A_{1,2} e^{3i\omega_D t}$	$u_{2,2} = 3A_{2,2} e^{3i\omega_D t}$ $\dot{u}_{2,2} = 9i\omega_D A_{2,2} e^{3i\omega_D t}$ $\ddot{u}_{2,2} = -27\omega_D^2 A_{2,2} e^{3i\omega_D t}$

(18)

From Eq. (18), we equate the multi-order vibration mode with the order of ϵ derived in Eq. (17). Using the substitution method, we can get all the amplitude of $A_{1,n-1}$ and $A_{2,n-1}$. At first, the zeroth order amplitudes are calculated as,

$$m\ddot{u}_{1,0} = k_1\left[\left(F_1 e^{i\omega_D t} - u_{1,0}\right) - \left(u_{1,0} - u_{2,0}\right)\right] - \eta\dot{u}_{1,0}$$

$$m\ddot{u}_{2,0} = k_1\left[\left(u_{1,0} - u_{2,0}\right) - \left(u_{2,0} - F_2 e^{i\omega_D t}\right)\right] - \eta\dot{u}_{2,0}$$

Applying $u_{1,0}$ and $u_{2,0}$ in Eq. (16), we find the simultaneous equation for the amplitude $A_{1,0}$ and $A_{2,0}$ as,

$$-m\omega_D^2 A_{1,0} e^{i\omega_D t} = k_1\left(F_1 e^{i\omega_D t} - A_{1,0} e^{i\omega_D t}\right) - k_1\left(A_{1,0} e^{i\omega_D t} - A_{2,0} e^{i\omega_D t}\right) - i\eta\omega_D A_{1,0} e^{i\omega_D t}$$

$$\Rightarrow -m\omega_D^2 A_{1,0} e^{i\omega_D t} = \left[k_1\left(F_1 - A_{1,0}\right) - k_1\left(A_{1,0} - A_{2,0}\right) - i\eta\omega_D A_{1,0}\right] e^{i\omega_D t}$$

$$\Rightarrow -m\omega_D^2 A_{1,0} = k_1\left(F_1 - A_{1,0}\right) - k_1\left(A_{1,0} - A_{2,0}\right) - i\eta\omega_D A_{1,0}$$

$$\Rightarrow (-m\omega_D^2 + 2k_1 + i\eta\omega_D)A_{1,0} - k_1 A_{2,0} = k_1 F_1$$

And

$$-m\omega_D^2 A_{2,0} e^{i\omega_D t} = k_1\left(A_{1,0} e^{i\omega_D t} - A_{2,0} e^{i\omega_D t}\right) - k_1\left(A_{2,0} e^{i\omega_D t} - F_2 e^{i\omega_D t}\right) - i\eta\omega_D A_{2,0} e^{i\omega_d t}$$

$$\Rightarrow -m\omega_D^2 A_{2,0} e^{i\omega_D t} = \left[-k_1\left(A_{2,0} - F_2\right) + k_1\left(A_{1,0} - A_{2,0}\right) - i\eta\omega_D A_{2,0}\right] e^{i\omega_D t}$$

$$\Rightarrow -m\omega_D^2 A_{1,0} = -k_1\left(A_{2,0} - F_2\right) + k_1\left(A_{1,0} - A_{2,0}\right) - i\eta\omega_D A_{2,0}$$

$$\Rightarrow -k_1 A_{1,0} + (-m\omega_D^2 + 2k_1 + i\eta\omega_D) A_{2,0} = k_1 F_2$$

We can rewrite the above equations in the compact form as such:

$$\begin{bmatrix} (-m\omega_D^2 + 2k_1 + i\eta\omega_D) & -k_1 \\ -k_1 & (-m\omega_D^2 + 2k_1 + i\eta\omega_D) \end{bmatrix} \begin{pmatrix} A_{1,0} \\ A_{2,0} \end{pmatrix} = \begin{pmatrix} k_1 F_1 \\ k_1 F_2 \end{pmatrix} \tag{19}$$

Simplifying,

$$\begin{pmatrix} A_{1,0} \\ A_{2,0} \end{pmatrix} = \frac{1}{(-m\omega_D^2 + 2k_1 + i\eta\omega_D)^2 - {k_1}^2} \begin{bmatrix} (-m\omega_D^2 + 2k_1 + i\eta\omega_D) & k_1 \\ k_1 & (-m\omega_D^2 + 2k_1 + i\eta\omega_D) \end{bmatrix} \begin{pmatrix} k_1 F_1 \\ k_1 F_2 \end{pmatrix}$$

Therefore,

$$A_{1,0} = \frac{F_1 k_1(-m\omega_D^2 + 2k_1 + i\eta\omega_D) + F_2 k_1^2}{(-m\omega_D^2 + 2k_1 + i\eta\omega_D)^2 - k_1^2}$$

$$A_{2,0} = \frac{F_1 k_1^2 + F_2 k_1(-m\omega_D^2 + 2k_1 + i\eta\omega_D)}{(-m\omega_D^2 + 2k_1 + i\eta\omega_D)^2 - k_1^2}$$

For the case of first-order amplitude, we get,

$$m\ddot{u}_{1,1} = k_1\left[\left(-u_{1,1}\right) - \left(u_{1,1} - u_{2,1}\right)\right] + k_2\left[\left(F_1 e^{i\omega_D t} - u_{1,0}\right)^2 - \left(u_{1,0} - u_{2,0}\right)^2\right] - \eta\dot{u}_{1,1}$$

$$m\ddot{u}_{2,1} = k_1\left[\left(u_{1,2} - u_{2,2}\right) - \left(u_{2,1}\right)\right] + k_2\left[\left(u_{1,0} - u_{2,0}\right)^2 - \left(u_{2,0} - F_2 e^{i\omega_D t}\right)^2\right] - \eta\dot{u}_{2,1}$$

Using the substitution method and applying the solution of u_1 and u_2 from Eq., we get,

$$-8m\omega_D^2 A_{1,1}e^{2i\omega_D t}$$

$$= k_1\left[\left(-2A_{1,1}e^{2i\omega_D t}\right) - \left(2A_{1,1}e^{2i\omega_D t} - 2A_{2,1}e^{2i\omega_D t}\right)\right]$$

$$+ k_2\left[\left(F_1 e^{i\omega_D t} - A_{1,0}e^{i\omega_D t}\right)^2 - \left(A_{1,0}e^{i\omega_D t} - A_{2,0}e^{i\omega_D t}\right)^2\right]$$

$$- 4i\eta\omega_D A_{1,1}e^{2i\omega_D t}$$

$$\Rightarrow -8m\omega_D^2 A_{1,1}e^{2i\omega_D t}$$

$$= k_1\left[\left(-2A_{1,1}\right) - 2\left(A_{1,1} - A_{2,1}\right)\right]e^{2i\omega_D t}$$

$$+ k_2\left[\left(F_1 - A_{1,0}\right)^2 - \left(A_{1,0} - A_{2,0}\right)^2\right]e^{2i\omega_D t} - 4i\eta\omega_D A_{1,1}e^{2i\omega_D t}$$

$$\Rightarrow -8m\omega_D^2 A_{1,1}$$

$$= k_1\left[\left(-2A_{1,1}\right) - 2\left(A_{1,1} - A_{2,1}\right)\right] + k_2\left[\left(F_1 - A_{1,0}\right)^2 - \left(A_{1,0} - A_{2,0}\right)^2\right]$$

$$- 4i\eta\omega_D A_{1,1}$$

$$\Rightarrow (-8m\omega_D^2 + 4k_1 + 4i\eta\omega_D)A_{1,1} - 2k_1 A_{2,1} = k_2\left[\left(F_1 - A_{1,0}\right)^2 - \left(A_{1,0} - A_{2,0}\right)^2\right]$$

And

$$-8m\omega_D^2 A_{2,1}e^{2i\omega_D t}$$

$$= k_1\left[\left(2A_{1,1}e^{2i\omega_D t} - 2A_{2,1}e^{2i\omega_D t}\right) - \left(2A_{2,1}e^{2i\omega_D t}\right)\right]$$

$$+ k_2\left[\left(A_{1,0}e^{i\omega_D t} - A_{2,0}e^{i\omega_D t}\right)^2 - \left(A_{2,0}e^{i\omega_D t} - F_2 e^{i\omega_D t}\right)^2\right]$$

$$- 4i\eta\omega_D A_{2,1}e^{2i\omega_D t}$$

$$\Rightarrow -8m\omega_D^2 A_{1,1} e^{2i\omega_D t}$$

$$= k_1\left[\left(2A_{1,1} - 2A_{2,1}\right) - \left(2A_{2,1}\right)\right] e^{2i\omega_D t}$$

$$+ k_2\left[\left(A_{1,0} - A_{2,0}\right)^2 + \left(A_{2,0} - F_2\right)^2\right] e^{2i\omega_D t} - 4i\eta\omega_D A_{2,1} e^{2i\omega_D t}$$

$$\Rightarrow -8m\omega_D^2 A_{\mathbf{2},1}$$

$$= k_1\left[2\left(A_{1,1} - A_{2,1}\right) - \left(2A_{2,1}\right)\right] + k_2\left[\left(A_{1,0} - A_{2,0}\right)^2 + \left(A_{2,0} - F_2\right)^2\right]$$

$$- 4i\eta\omega_D A_{2,1}$$

$$\Rightarrow -2k_1 A_{1,1} + (-8m\omega_D^2 + 4k_1 + 4i\eta\omega_D) A_{2,1} = k_2\left[\left(A_{1,0} - A_{2,0}\right)^2 + \left(A_{2,0} - F_2\right)^2\right]$$

Using elimination method, we get,

$$A_{1,1} = \frac{1}{(-8m\omega_D^2 + 4k_1 + 4i\eta\omega_D)^2 - 4k_1^2}\Big[2k_1 k_2\left(\left(A_{1,0} - A_{2,0}\right)^2 + \left(A_{2,0} - F_2\right)^2\right)$$

$$+ k_2\left(\left(F_1 - A_{1,0}\right)^2 - \left(A_{1,0} - A_{2,0}\right)^2\right)(-8m\omega_D^2 + 4k_1 + 4i\eta\omega_D)\Big]$$

$$A_{2,1} = \frac{1}{(-8m\omega_D^2 + 4k_1 + 4i\eta\omega_D)^2 - 4k_1^2}\Big[2k_1 k_2\left[\left(F_1 - A_{1,0}\right)^2 - \left(A_{1,0} - A_{2,0}\right)^2\right]$$

$$+ k_2\left(\left(A_{1,0} - A_{2,0}\right)^2 + \left(A_{2,0} - F_2\right)^2\right)(-8m\omega_D^2 + 4k_1 + 4i\eta\omega_D)\Big]$$

For the case of second order amplitude, we get,

$$m\ddot{u}_{1,2} = k_1\left[\left(-u_{1,2}\right) - \left(u_{1,2} - u_{2,2}\right)\right] + k_2\left(-2F_1 e^{i\omega_D t} u_{1,1} + 2u_{1,0}u_{1,1}\right)$$

$$- k_2\left(2u_{1,0}u_{1,1} - 2u_{1,1}u_{2,0} - 2u_{1,0}u_{2,1} + 2u_{2,0}u_{2,1}\right)$$

$$+ k_3\left[\left(F_1 e^{i\omega_D t} - u_{1,0}\right)^3 - \left(u_{1,0} - u_{2,0}\right)^3\right] - \eta\dot{u}_{1,2}$$

$$m\ddot{u}_{2,2} = k_1\left[\left(u_{1,2} - u_{2,2}\right) - \left(u_{2,2}\right)\right] + k_2\left(2F_2e^{i\omega_D t}u_{2,1} - 2u_{2,0}u_{2,1}\right)$$
$$+ k_2\left(2u_{1,0}u_{1,1} - 2u_{1,1}u_{2,0} - 2u_{1,0}u_{2,1} + 2u_{2,0}u_{2,1}\right)$$
$$+ k_3\left[\left(u_{1,0} - u_{2,0}\right)^3 - \left(u_{2,0} - F_2e^{i\omega_D t}\right)^3\right] - \eta\dot{u}_{2,2}$$

Substituting u_1 and u_2 from Eq. (18), we get,

$$-27m\omega_D^2A_{1,2}e^{3i\omega_D t}$$
$$= k_1\left[\left(-3A_{1,2}e^{3i\omega_D t}\right) - \left(3A_{1,2}e^{3i\omega_D t} - 3A_{2,2}e^{3i\omega_D t}\right)\right]$$
$$+ k_2\left(-4F_1e^{i\omega_D t}A_{1,1}e^{2i\omega_D t} + 4A_{1,0}e^{i\omega_D t}A_{1,1}e^{2i\omega_D t}\right)$$
$$- k_2\left(4A_{1,0}e^{i\omega_D t}A_{1,1}e^{2i\omega_D t} - 4A_{1,1}e^{2i\omega_D t}A_{1,0}e^{i\omega_D t} - 4A_{1,0}e^{i\omega_D t}A_{2,1}e^{2i\omega_D t}\right.$$
$$\left. + 4A_{2,0}e^{i\omega_D t}A_{2,1}e^{2i\omega_D t}\right)$$
$$+ k_3\left[\left(F_1e^{i\omega_D t} - A_{1,0}e^{i\omega_D t}\right)^3 - \left(A_{1,0}e^{i\omega_D t} - A_{2,0}e^{i\omega_D t}\right)^3\right]$$
$$- 9i\eta\omega_D A_{1,2}e^{3i\omega_D t}$$

$$\Rightarrow -27m\omega_D^2A_{1,2}e^{3i\omega_D t}$$
$$= k_1\left[\left(-3A_{1,2}\right) - 3\left(A_{1,2} - A_{2,2}\right)\right]e^{3i\omega_D t} + 4k_2\left(-F_1A_{1,1} + A_{1,0}A_{1,1}\right)e^{3i\omega_D t}$$
$$- 4k_2\left(A_{1,0}A_{1,1} - A_{1,1}A_{1,0} - A_{1,0}A_{2,1} + A_{2,0}A_{2,1}\right)e^{3i\omega_D t}$$
$$+ k_3\left[\left(F_1 - A_{1,0}\right)^3 - \left(A_{1,0} - A_{2,0}\right)^3\right]e^{3i\omega_D t} - 9i\eta\omega_D A_{1,2}e^{3i\omega_D t}$$

$$\Rightarrow -27m\omega_D^2A_{1,2}$$
$$= k_1\left[\left(-3A_{1,2}\right) - 3\left(A_{1,2} - A_{2,2}\right)\right]$$
$$+ 4k_2\left(-F_1A_{1,1} - A_{1,1}A_{1,0} - A_{1,0}A_{2,1} + A_{2,0}A_{2,1}\right)$$
$$+ k_3\left[\left(F_1 - A_{1,0}\right)^3 - \left(A_{1,0} - A_{2,0}\right)^3\right] - 9i\eta\omega_D A_{1,2}$$

$$\Rightarrow (-27m\omega_D^2 + 6k_1 + 9i\eta\omega_D)A_{1,2} - 3k_1A_{2,2}$$

$$= 4k_2\left(-F_1A_{1,1} - A_{1,1}A_{1,0} - A_{1,0}A_{2,1} + A_{2,0}A_{2,1}\right)$$

$$+ k_3\left[\left(F_1 - A_{1,0}\right)^3 - \left(A_{1,0} - A_{2,0}\right)^3\right]$$

And,

$$-27m\omega_D^2A_{2,2}e^{3i\omega_Dt}$$

$$= k_1\left[\left(3A_{1,2}e^{3i\omega_Dt} - 3A_{2,2}e^{3i\omega_Dt}\right) - \left(3A_{2,2}e^{3i\omega_Dt}\right)\right]$$

$$+ k_2\left(4F_2e^{i\omega_Dt}A_{2,1}e^{2i\omega_Dt} - 4A_{2,0}e^{i\omega_Dt}A_{2,1}e^{2i\omega_Dt}\right)$$

$$+ k_2\left(4A_{1,0}e^{i\omega_Dt}A_{1,1}e^{2i\omega_Dt} - 4A_{1,1}e^{2i\omega_Dt}A_{2,0}e^{i\omega_Dt} - 4A_{1,0}e^{i\omega_Dt}A_{2,1}e^{2i\omega_Dt}\right.$$

$$\left. + 4A_{2,0}e^{i\omega_Dt}A_{2,1}e^{2i\omega_Dt}\right)$$

$$+ k_3\left[\left(A_{1,0}e^{i\omega_Dt} - A_{2,0}e^{i\omega_Dt}\right)^3 + \left(A_{2,0}e^{i\omega_Dt} - F_2e^{i\omega_Dt}\right)^3\right]$$

$$- 9i\eta\omega_DA_{2,2}e^{3i\omega_Dt}$$

$$\Rightarrow -27m\omega_D^2A_{2,2}e^{3i\omega_Dt}$$

$$= k_1\left[3\left(A_{1,2} - A_{2,2}\right) - \left(3A_{2,2}\right)\right]e^{3i\omega_Dt} + 4k_2\left(F_2A_{2,1} - A_{2,0}A_{2,1}\right)e^{3i\omega_Dt}$$

$$+ 4k_2\left(A_{1,0}A_{1,1} - A_{1,1}A_{2,0} - A_{1,0}A_{2,1} + A_{2,0}A_{2,1}\right)e^{3i\omega_Dt}$$

$$+ k_3\left[\left(A_{1,0} - A_{2,0}\right)^3 + \left(A_{2,0} - F_2\right)^3\right]e^{3i\omega_Dt} - 9i\eta\omega_DA_{2,2}e^{3i\omega_Dt}$$

$$\Rightarrow -27m\omega_D^2 A_{2,2}$$

$$= k_1\left[3\left(A_{1,2} - A_{2,2}\right) - \left(3A_{2,2}\right)\right]$$

$$+ 4k_2\left(F_2A_{2,1} + A_{1,0}A_{1,1} - A_{1,1}A_{2,0} - A_{1,0}A_{2,1}\right)$$

$$+ k_3\left[\left(A_{1,0} - A_{2,0}\right)^3 + \left(A_{2,0} - F_2\right)^3\right] - 9i\eta\omega_D A_{2,2}$$

$$\Rightarrow -3k_1A_{1,2} + (-27m\omega_D^2 + 6k_1 + 9i\eta\omega_D)A_{2,2}$$

$$= 4k_2\left(F_2A_{2,1} + A_{1,0}A_{1,1} - A_{1,1}A_{2,0} - A_{1,0}A_{2,1}\right)$$

$$+ k_3\left[\left(A_{1,0} - A_{2,0}\right)^3 + \left(A_{2,0} - F_2\right)^3\right]$$

Using elimination method, we get,

$$A_{1,2} = \frac{1}{(-27m\omega_D^2 + 6k_1 + 9i\eta\omega_D)^2 - 9k_1^2}\Big[12k_1k_2\left(F_2A_{2,1} + A_{1,0}A_{1,1} - A_{1,1}A_{2,0} - A_{1,0}A_{2,1}\right)$$

$$+ 3k_1k_3\left(\left(A_{1,0} - A_{2,0}\right)^3 - \left(A_{2,0} - F_2\right)^3\right)$$

$$+ \Big(4k_2\left(-F_1A_{1,1} + A_{1,1}A_{2,0} - A_{1,0}A_{2,1} + A_{2,0}A_{2,1}\right)$$

$$+ k_3\left(\left(F_1 - A_{1,0}\right)^3 - \left(A_{1,0} - A_{2,0}\right)^3\right)\Big)(-27m\omega_D^2 + 6k_1 + 9i\eta\omega_D)\Big]$$

$$A_{2,2} = \frac{1}{(-27m\omega_D^2 + 6k_1 + 9i\eta\omega_D)^2 - 9k_1^2}\Big[12k_1k_2\left(-F_1A_{1,1} + A_{1,1}A_{2,0} - A_{1,0}A_{2,1} + A_{2,0}A_{2,1}\right)$$

$$+ 3k_1k_3\left(\left(F_1 - A_{1,0}\right)^3 - \left(A_{1,0} - A_{2,0}\right)^3\right)$$

$$+ \Big(4k_2\left(F_2A_{2,1} + A_{1,0}A_{1,1} - A_{1,1}A_{2,0} - A_{1,0}A_{2,1}\right)$$

$$+ k_3\left(\left(A_{1,0} - A_{2,0}\right)^3 + \left(A_{2,0} - F_2\right)^3\right)\Big)(-27m\omega_D^2 + 6k_1 + 9i\eta\omega_D)\Big]$$

We can replace the common terms with $\gamma_1, \gamma_2, \gamma_3, \sigma_1, \sigma_2, \sigma_3, \sigma_4, \sigma_5, \sigma_6$, which gives us the amplitude as in Eq. (20).

$$A_{1,0} = \frac{F_1 k_1 \gamma_1 + F_2 k_1^2}{{\gamma_1}^2 - k_1^2}, \qquad A_{2,0} = \frac{F_1 k_1^2 + F_2 k_1 \gamma_1}{{\gamma_1}^2 - k_1^2}$$

$$A_{1,1} = \frac{2k_1 k_2 \sigma_1 + k_2 \gamma_2 \sigma_2}{{\gamma_2}^2 - 4k_1^2}, \qquad A_{2,1} = \frac{2k_1 k_2 \sigma_2 + k_2 \gamma_2 \sigma_1}{{\gamma_2}^2 - 4k_1^2}$$

$$A_{1,2} = \frac{12k_1 k_2 \sigma_5 + 3k_1 k_3 \sigma_3 + 4k_2 \gamma_3 \sigma_6 + k_3 \gamma_3 \sigma_4}{{\gamma_3}^2 - 9k_1^2},$$

$$A_{2,2} = \frac{12k_1 k_2 \sigma_6 + 3k_1 k_3 \sigma_4 + 4k_2 \gamma_3 \sigma_5 + k_3 \gamma_3 \sigma_3}{{\gamma_3}^2 - 9k_1^2} \tag{20}$$

Here $A_{1,n-1}$ and $A_{2,n-1}$ represent amplitudes of the granules at the characteristic frequency $n\omega_D$. For example, $A_{1,0}$ and $A_{2,0}$ represent the amplitude response at the driving frequency ω_D, while $A_{1,1}, A_{2,1}, A_{1,2}$ and $A_{2,2}$ represent the higher harmonic amplitude response at the other characteristic frequencies $(2\omega_D, 3\omega_D)$ due to the nonlinear term of Eq. (16). The above perturbation technique reveals the amplitudes at each of the characteristic frequency $n\omega_D$ of the nonlinear network of Eq. (16). In the current study, we have limited the perturbation method until the second order of minor term ϵ, where the zeroth-order amplitude represents the linearized term, and the first- and second-order amplitudes are the nonlinear responses of the system. Yet, the technique can be expanded to include higher-order terms.

3. DEFINITION AND DEMONSTRATION OF NONLINEAR NORMAL MODE IN CLASSICAL GRANULAR MEDIUM AND CONTROL THROUGH EXTERNAL EXCITATION

The study of oscillatory dynamics in nonlinear systems is a cornerstone of understanding energy transfer, wave behavior, and coherent structures in a wide range of physical media. In granular systems, where interactions are inherently nonlinear and non-cohesive, traditional linear modal analysis falls short of capturing the full dynamic richness. This necessitates the introduction of Nonlinear Normal Modes (NNMs), a generalization of linear normal modes tailored to nonlinear and often discontinuous systems.

Nonlinear Normal Modes provide a robust framework for analyzing complex vibratory behaviors where superposition is no longer applicable and modal interactions become energy-dependent and structurally rich.

3.1. Definition and Mathematical Foundations:

In linear systems, a normal mode is defined as a synchronous oscillation where all degrees of freedom oscillate harmonically at a standard natural frequency. These modes are orthogonal and form a complete basis for representing system dynamics. In contrast, Nonlinear Normal Modes are defined as families of periodic solutions in nonlinear dynamical systems where all state variables exhibit the same periodicity — but not necessarily in a synchronized or sinusoidal manner.

Mathematically, consider a general autonomous, conservative, discrete mechanical system governed by:

$$\ddot{u} + f(u) = 0 \tag{21}$$

where $u \in \mathbb{R}^n$ is the displacement vector, and $f(u)$ denotes the nonlinear restoring force. A Nonlinear Normal Mode is a periodic solution $u(t) = \phi(t)$, such as:

- $\phi(t)$ is a T-periodic function for some $T > 0$.
- All system components oscillate with the same fundamental frequency $\omega = \frac{2\pi}{T}$.
- The trajectory lies on a two-dimensional invariant manifold in phase space, which is parameterized by the amplitude and phase of the oscillation.

Unlike linear modes, NNMs are not orthogonal, and their frequencies vary with energy. The mode shape itself can deform as the amplitude increases, leading to modal bending, bifurcation, and localization.

3.1.1. Characteristics in Granular Media:

Granular crystals, especially those composed of identical or alternating elastic spheres, are ideal testbeds for exploring NNMs due to the Hertzian nonlinearity in their contact mechanics. The governing contact force between two granules is given by:

$$F = k_{NL}(\delta + \delta_0)^{3/2} \tag{22}$$

This leads to nonlinear and potentially non-smooth equations of motion, especially in the absence of precompression (i.e., the sonic vacuum regime).

Under weak precompression, the system supports weakly nonlinear NNMs, where the frequency dependence on amplitude is moderate. In contrast, when precompression is absent or minimal, the system becomes strongly nonlinear, and energy is transferred nonlinearly among different degrees of freedom, often exhibiting mode localization or energy trapping.

A key feature of NNMs in such media is the loss of modal superposition. In a linear system, any linear combination of modes is also a solution [50]. However, in granular chains, the nonlinear coupling causes modes to interact and evolve in complex ways, often leading to energy exchange, spectral broadening, and modal modulation.

3.1.2. Classifications of Nonlinear Normal Modes:

In granular chains, NNMs can be classified based on phase relationships and symmetry:

- **In-Phase NNMs:** All particles oscillate synchronously with identical phases. These modes are typically associated with longitudinal oscillations where compression and extension occur uniformly.
- **Out-of-Phase NNMs:** Particles oscillate with alternating phases, e.g., neighboring particles are π out of phase. These correspond to optical-like modes in diatomic systems or to higher-order internal dynamics in homogeneous chains.
- **Localized NNMs (Discrete Breathers):** Due to strong nonlinearity and spatial discreteness, some modes can become spatially localized — energy remains confined to a small region of the chain. These breathers do not radiate energy and persist over long timescales.

The existence of these mode types depends on system parameters such as precompression, mass distribution (e.g., in dimer or trimer chains), and boundary conditions.

3.1.3. Energy Dependence and Frequency-Energy Plots (FEPs):

One of the defining features of NNMs is the nonlinear relationship between energy and frequency. As energy increases, the frequency of a given NNM deviates from its linear value, often leading to bifurcations or modal transitions [51].

This behavior is captured in Frequency-Energy Plots (FEPs), which map the frequency of oscillation versus the total energy of the mode. In granular systems:

- The in-phase NNM typically marks the lower bound of the FEP.
- The out-of-phase NNM lies at the upper-frequency limit.
- Between them lies a propagation zone where frequencies correspond to extended oscillations.
- Outside these bounds, particularly beyond the out-of-phase NNM, lies the attenuation zone, where responses become localized or decay rapidly.

FEPs not only visualize nonlinear dynamics but also help identify parameter regimes where specific NNMs dominate or coexist.

3.2. Nonlinear Normal Modes in Classical Two-Mass Granular Network:

Following the general classification of Nonlinear Normal Modes (NNMs), we now examine their manifestation in a simple yet insightful nonlinear granular network composed of two interacting granules. This minimal model—although limited in size—captures the essential dynamics of NNMs by leveraging the Hertzian contact law, allowing for the identification of distinct modal behaviors, particularly the in-phase and out-of-phase modes [52].

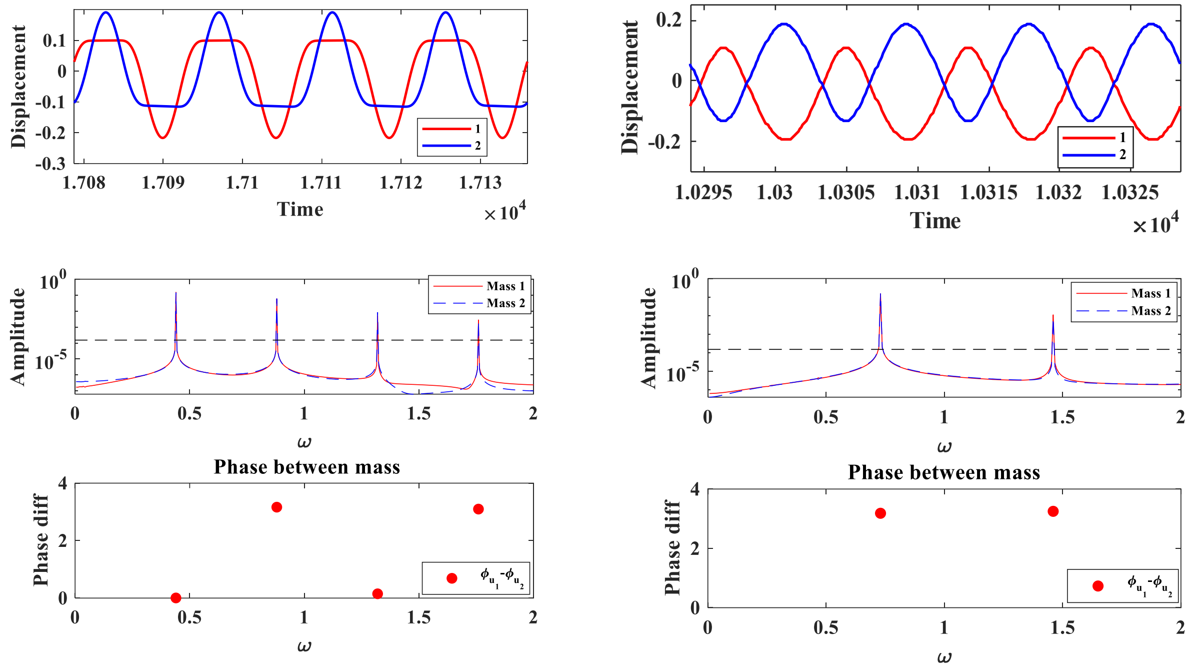

Figure 4: Time-domain displacement, frequency response, and phase difference between two granules in a nonlinear granular network exhibiting Nonlinear Normal Modes (NNMs). The left column illustrates the in-phase NNM at driving frequency ($\omega_D = 0.45$), where both masses oscillate synchronously with zero phase difference, a characteristic of lower-frequency excitation and intermittent contact. The right column shows the out-of-phase NNM ($\omega_D = 0.73$), with masses oscillating in anti-symmetry (π phase difference), corresponding to higher frequency excitation and sustained contact. The responses are obtained under strongly nonlinear conditions with no static precompression ($\delta_0 = 0$), revealing distinct modal structures governed by Hertzian interactions.

Together, these two NNMs, the in-phase and out-of-phase modes—demonstrate how even a simple two-particle granular system governed by nonlinear, unilateral Hertzian contact laws can support rich, energy-dependent modal structures. The nature of coupling, the lack of tensile strength, and the frequency-dependent excitation all contribute to the emergence of these distinct behaviors. Notably, the level of static precompression plays a critical role in shaping the system's nonlinearity when precompression is absent. $(\delta_0 = 0)$ The system operates in a highly nonlinear regime, where contact is intermittent, and forces vanish when particles are separated. Conversely, introducing precompression smooths out these interactions and shifts the system toward a weakly nonlinear regime, where continuous contact leads to more regular, near-harmonic behavior. These distinctions are essential in determining modal behavior, resonance structure, and energy transmission characteristics. From this point forward, we will examine how varying levels of nonlinearity—ranging from weak to vigorous—affect the dynamical response of the system and influence phenomena such as mode localization, energy trapping, and classical analogs of modal superposition.

The in-phase NNM is defined by the synchronous oscillation of the two granules—meaning both masses reach their maximum and minimum displacements simultaneously. This behavior is evident in **Figure 4** on the left-hand side of the provided figure. In the top subplot, the red and blue displacement curves corresponding to masses 1 and 2, respectively, are seen to rise and fall in unison. This synchronous motion reflects the symmetric nature of the mode, suggesting that the relative displacement between the masses remains minimal, which leads to intermittent contact or near-contact dynamics due to the non-tensile nature of Hertzian interactions. This periodic engagement and disengagement between particles are key characteristics of the in-phase mode in uncompressed granular networks.

In the middle subplot of the **Figure 4** the left-hand panel, the frequency-domain response is shown by plotting the amplitude spectrum of each mass. Here, both masses exhibit resonant peaks at the same frequencies, confirming that they are being excited and responding in a coherent manner. Notably, the amplitude remains high across several harmonics, which is indicative of the nonlinear nature of the contact interaction—higher-order harmonics are generated due to the nonlinear force-displacement relationship. This frequency response further substantiates the interpretation that the system behaves collectively in this regime. The bottom subplot reinforces this conclusion: it plots the phase difference between the two mass responses at various excitation frequencies. A near-zero phase difference across the primary and harmonic resonances indicates that the oscillators are indeed synchronized, confirming the in-phase modal structure.

Contrastingly, the out-of-phase NNM represents a fundamentally different oscillatory state. This mode is characterized by anti-symmetric motion, where one mass moves in the opposite direction to the other—when one granule reaches its peak, the other hits a trough. This behavior, shown on the **Figure 4**: right-hand side of the figure is represented in the top subplot by displacement curves that are almost perfect mirror images of each other over time. The anti-symmetric motion implies that the relative displacement between the two masses is maximized during the oscillation cycle, ensuring continuous contact and force transmission even without static precompression. This leads to smoother and more persistent energy exchange through Hertzian contact, a hallmark of the out-of-phase configuration.

The middle frequency-domain plot of the **Figure 4** right panel shows a strong resonant peak, similar to the in-phase case, but centered at a higher excitation frequency. This shift to higher frequency is expected, as out-of-phase modes typically correspond to higher energy configurations and emerge prominently under higher driving frequencies. Here, both masses still respond at the same frequency, but their relative motions are opposite in sign. This is confirmed in the bottom subplot, which shows a consistent phase difference close to π, affirming that the masses oscillate in anti-phase. This persistent phase shift is a defining feature of the out-of-phase NNM, distinguishing it from other, more complex nonlinear modal interactions.

Together, these two NNMs—the in-phase and out-of-phase modes—demonstrate how even a simple two-particle granular system governed by nonlinear, unilateral Hertzian contact laws can support rich, energy-dependent modal structures. The nature of coupling, the lack of tensile strength, and the frequency-dependent excitation all contribute to the emergence of these distinct behaviors. These modes form the basis for interpreting modal superposition, energy localization, and phase-encoded logic in larger granular arrays. In later sections, we will explore how these fundamental NNMs serve as analogs for classical bit states and can be leveraged to construct higher-level dynamical logic operations within nonlinear metamaterials.

4. ILLUSTRATION OF ELASTIC BIT: MATHEMATICAL MODELLING OF THE CLASSICAL ANALOGOUS SUPERPOSTION OF STATES COEFFICIENT OF COMPLEX AMPLITUDE

4.1. Eigenmodes of Granular Network:

To implement the orthonormal basis of the total displacement field $\vec{U}$. We obtain the linear eigenstates from the zeroth-order displacement response of the granular network [53-55]. From Eq. (19), by taking the real part of the stiffness matrix K, the eigenmode frequencies is calculated as $\det(K) = 0$, which gives us the eigenmode frequencies as, $\omega_{01}^2 = \sqrt{\frac{k_1}{m}}$ and $\omega_{02}^2 = \sqrt{\frac{3k_1}{m}}$. To obtain the eigenstates, we apply the eigenmode frequencies as given in Eq. (19), When $\omega_D = \omega_{01} = \sqrt{\frac{k_1}{m}}$,

$$\begin{bmatrix} -m\dfrac{k_1}{m} + 2k_1 & -k_1 \\ -k_1 & -m\dfrac{k_1}{m} + 2k_1 \end{bmatrix} \begin{pmatrix} A_{1,0} \\ A_{2,0} \end{pmatrix} = 0 \Rightarrow \begin{bmatrix} k_1 & -k_1 \\ -k_1 & k_1 \end{bmatrix} \begin{pmatrix} A_{1,0} \\ A_{2,0} \end{pmatrix} = 0$$

$$\Rightarrow k_1 \begin{bmatrix} 1 & -1 \\ -1 & 1 \end{bmatrix} \begin{pmatrix} A_{1,0} \\ A_{2,0} \end{pmatrix} = 0$$

Both equations yield the same results, namely, $A_{1,0} = A_{2,0}$. So, $\begin{pmatrix} A_{1,0} \\ A_{2,0} \end{pmatrix}$ is proportional to the vector $\begin{pmatrix} 1 \\ 1 \end{pmatrix}$. After normalization, we get the eigenstate corresponding to ω_{01} as $E_1 = \frac{1}{\sqrt{2}}\begin{pmatrix} 1 \\ 1 \end{pmatrix}$.

When $\omega_D = \omega_{01} = \sqrt{\frac{3k_1}{m}}$,

$$\begin{bmatrix} -m\dfrac{3k_1}{m} + 2k_1 & -k_1 \\ -k_1 & -m\dfrac{3k_1}{m} + 2k_1 \end{bmatrix} \begin{pmatrix} A_{1,0} \\ A_{2,0} \end{pmatrix} = 0 \Rightarrow \begin{bmatrix} -k_1 & -k_1 \\ -k_1 & -k_1 \end{bmatrix} \begin{pmatrix} A_{1,0} \\ A_{2,0} \end{pmatrix} = 0$$

$$\Rightarrow k_1 \begin{bmatrix} -1 & -1 \\ -1 & -1 \end{bmatrix} \begin{pmatrix} A_{1,0} \\ A_{2,0} \end{pmatrix} = 0$$

So, the equations give us $A_{1,0} = -A_{2,0}$. So, $\begin{pmatrix} A_{1,0} \\ A_{2,0} \end{pmatrix}$ is proportional to vector $\begin{pmatrix} 1 \\ -1 \end{pmatrix}$. After normalization, we get the eigenstate corresponding to ω_{02} as $E_1 = \frac{1}{\sqrt{2}}\begin{pmatrix} 1 \\ -1 \end{pmatrix}$. This E_1 and E_2 demonstrates the eigenstates of a linearized granular network. These are the corresponding in-phase and out-of-phase modes of the system.

4.2. Formation of the Superposition of States:

The investigation of classical systems that replicate quantum phenomena presents a fascinating new avenue for understanding how complex systems behave when subjected to external influences. A method for comprehending the dynamics of displacements in a granular system (shown as u_1 and, u_2) under external forces was introduced in the preceding section. These displacements were represented as the sum of linear and nonlinear modes, each with a unique frequency, ω_n. Our perturbation techniques enabled us to derive these frequencies. The displacements u_1 and u_2 are roughly represented as follows:

$$u_1 = \sum_{n=1}^{3} \epsilon^{n-1} u_{1,n-1} = \sum_{n=1}^{3} \epsilon^{n-1} nA_{1,n-1} e^{ni\omega_D t}, u_2 = \sum_{n=1}^{3} \epsilon^{n-1} u_{2,n-1} = \sum_{n=1}^{3} \epsilon^{n-1} nA_{2,n-1} e^{ni\omega_D t}$$

where ϵ denotes a small parameter dictating the strength of the nonlinearities. These modes reflect the granular system's response to external excitations at different characteristic frequencies. For each frequency, the displacement field can be expressed in a linear normal mode basis with complex coefficients, leading to the following expression:

$$\begin{pmatrix} nA_{1,n-1} \\ nA_{2,n-1} \end{pmatrix} e^{ni\omega_D t} \equiv (\alpha_n |E_1\rangle + \beta_n |E_2\rangle) e^{ni\omega_D t} \tag{23}$$

Here, $E_1 = \frac{1}{\sqrt{2}}\begin{pmatrix} 1 \\ 1 \end{pmatrix}$ and $E_2 = \frac{1}{\sqrt{2}}\begin{pmatrix} 1 \\ -1 \end{pmatrix}$, represent the in-phase and out-of-phase eigenmodes of the linearized granular system. The coefficients α_n and β_n are complex amplitudes corresponding to the contributions of each eigenmode E_1 or E_2, respectively. These coefficients satisfy the normalization condition $|\alpha_n|^2 + |\beta_n|^2 = 1$. When $\alpha_n = 1, \beta_n = 0$, and vice versa, the system is in a pure eigenstate, either E_1 or E_2. In other cases, a linear superposition of these eigenmodes occurs, forming a superposition state.

While the nonlinear modes do not directly contribute to the orthonormal properties of a system, the combination of E_1 and E_2 forms a complete orthonormal basis for the granular system. Therefore, using the analogy to quantum mechanics, we apply Dirac notation for the state vectors, as shown in Eq. (23). This representation enables us to calculate the coefficients α_n and β_n from the displacement field:

$$\alpha_n = \frac{\left(A_{1,n-1} + A_{2,n-1}\right)}{\sqrt{2}}; \quad \beta_n = \frac{\left(A_{1,n-1} - A_{2,n-1}\right)}{\sqrt{2}}$$

Using Eq. (20), we get:

$$\alpha_1 = \frac{1}{\sqrt{2}} \frac{k_1(F_1 + F_2)}{(\gamma_1 - k_1)}, \qquad \beta_1 = \frac{1}{\sqrt{2}} \frac{k_1(F_1 - F_2)}{(\gamma_1 + k_1)}$$

$$\alpha_2 = \frac{1}{\sqrt{2}} \frac{k_2(\sigma_1 + \sigma_2)}{(\gamma_2 - 2k_1)}, \qquad \beta_2 = \frac{1}{\sqrt{2}} \frac{k_2(\sigma_1 - \sigma_2)}{(\gamma_2 + 2k_1)}$$

$$\alpha_3 = \frac{1}{\sqrt{2}} \frac{4k_2(\sigma_5 + \sigma_6) + k_3(\sigma_3 + \sigma_4)}{\gamma_3 - 3k_1}, \quad \beta_3 = \frac{1}{\sqrt{2}} \frac{4k_2(\sigma_6 - \sigma_5) + k_3(\sigma_4 - \sigma_3)}{\gamma_3 + 3k_1} \tag{24}$$

In this context, Dirac-ket notation is employed to concisely and effectively capture the state of the classical granular system as it evolves under external driving forces. Because the system's response can be projected onto a two-dimensional Hilbert space formed by the in-phase and out-of-phase eigenmodes, this notation offers a structured way to represent the state as a time-dependent superposition of these modes. Using $|E_1\rangle$ and $|E_2\rangle$ as basis vectors, the full vibrational state $|\psi(t)\rangle$ becomes a compact expression that preserves both amplitude and phase information.

This formulation is potent because it mirrors the language of quantum systems, allowing the classical system to be analyzed using tools developed for quantum mechanics, such as coherence, normalization, and phase relationships. In this case, it means that the nonlinear oscillatory response of the granular network can be represented as a single evolving state vector, allowing for a direct analogy to qubit behavior and enabling the exploration of classical superposition, coherent control, and geometric phase accumulation within a well-defined mathematical framework. Using these definitions, we can express the total displacement field as a linear superposition of E_1 and E_2, leading to the following form:

$$\begin{aligned}\vec{U} = \begin{pmatrix} u_1 \\ u_2 \end{pmatrix} &= \sum_{n=1}^{3} \begin{pmatrix} \epsilon^{n-1} n A_{1,n-1} \\ \epsilon^{n-1} n A_{2,n-1} \end{pmatrix} e^{ni\omega_D t} \\ &\equiv \epsilon^0([\alpha_1|E_1\rangle + \beta_1|E_2\rangle])e^{i\omega_D t} + \epsilon^1([\alpha_2|E_1\rangle + \beta_2|E_2\rangle])e^{2i\omega_D t} \\ &+ \epsilon^2([\alpha_3|E_1\rangle + \beta_3|E_2\rangle])e^{3i\omega_D t} \equiv \left[\tilde{\alpha}(t)|E_1\rangle + \tilde{\beta}(t)|E_2\rangle\right] \end{aligned} \tag{25}$$

Here, $\tilde{\alpha}(t) = \left(\sum_{n=1}^{3} \epsilon^{n-1}\alpha_n e^{ni\omega_D t}\right) / \left(\sqrt{|\sum_{n=1}^{3} \epsilon^{n-1}\alpha_n e^{ni\omega_D t}|^2 + |(\sum_{n=1}^{3} \epsilon^{n-1}\beta_n e^{ni\omega_D t})|^2}\right)$ and $\tilde{\beta}(t) = \left(\sum_{n=1}^{3} \epsilon^{n-1}\beta_n e^{ni\omega_D t}\right) / \left(\sqrt{|\sum_{n=1}^{3} \epsilon^{n-1}\alpha_n e^{ni\omega_D t}|^2 + |(\sum_{n=1}^{3} \epsilon^{n-1}\beta_n e^{ni\omega_D t})|^2}\right)$. On that basis, the modal contribution in the mode superposition of the total displacement field can be written in the form of a column displacement state vector, $|\psi\rangle$ [32, 56]:

$$|\psi\rangle = \begin{pmatrix} \psi_0 \\ \psi_1 \end{pmatrix} = \begin{pmatrix} \displaystyle\sum_n \frac{1}{\sqrt{|\alpha_n|^2 + |\beta_n|^2}} \alpha_n e^{i\omega_n t} \\ \displaystyle\sum_n \frac{1}{\sqrt{|\alpha_n|^2 + |\beta_n|^2}} \beta_n e^{i\omega_n t} \end{pmatrix} = \begin{pmatrix} \tilde{\alpha}(t) \\ \tilde{\beta}(t) \end{pmatrix}. \tag{26}$$

where $\phi_\alpha = \tan^{-1}\left(\frac{\eta\omega}{m\omega_1^2 - m\omega^2}\right)$ and $\phi_\beta = \tan^{-1}\left(\frac{\eta\omega}{m\omega_2^2 - m\omega^2}\right)$; m is the mass of the granule, η is the system damping, and ω_1 and ω_2 are the eigen frequencies of the in-phase and out-of-phase modes of the eigen vectors of the linearized granular system The vibrations of the granules are represented by Eq. (25) projected into the two possible modes of vibration. The components of Eq. (25) are dependent on each other through the phase and form a coherent superposition of states in the space of two possible forms of vibration; since in-phase (E_1) and out-of-phase (E_2) vibration modes are physically distinguishable independent states [57, 58]. Moreover, the components of Eq. (25) physically correspond to superposed states, i.e., the characteristics of a pure in-phase eigenstate for $\phi_\beta - \phi_A = 0$ and the characteristics of a pure out-of-phase eigenstate for $\phi_\beta - \phi_A = \pi$. In contrast to classical mixed states or classical nonseparable combinations of longitudinal and torsional/shear modes, the superposition of states of Eq. (25) is coherent through the phase. We defined coherent states as states that retain their superposition characteristic, such that, the E_1 and E_2 eigenstates have a constant phase and exhibit interference for a given time instant. Moreover, over time, the coherent state stays coherent, but its phase relation evolves in time [59]. The superposition of states of Eq. (25) is also different than the problems that fall into a class that is nonseparable classically, where the nonseparability stems from media corners and crack edges.

The time-dependent coefficients, $\tilde{\alpha}(t)$ and $\tilde{\beta}(t)$ are normalized such that their total magnitude remains unity. Interestingly, while the coefficients α_n and β_n are time-independent, the coefficients $\tilde{\alpha}(t)$ and $\tilde{\beta}(t)$ evolve, reflecting the coherent nature of the system. These coefficients, as they change in time, determine the relative phase between the states, demonstrating how the granules' vibrational response can exhibit quantum-like behavior, even in a classical system.

The behavior of this system resembles that seen in quantum mechanics, where a quantum bit, or qubit, is defined as a superposition of two basis states. In quantum mechanics, a unit vector that characterizes a pure state is used to represent a qubit's state in a two-dimensional Hilbert space. The superposition of the eigenmodes E_1. and E_2. can also be represented by a unit vector in a two-dimensional complex vector space, which is comparable to a qubit and can be used to model the elastic bit in this classical system.

4.3. Time-Independent Formulation of Elastic Bit:

By employing the elimination and substitution method on the simultaneous amplitude equations we derive the complex amplitude solutions $A_{1,0}$ and $A_{2,0}$ in Eq. (19),

$$A_1 = \frac{F_1 k_L(-m\omega_D^2 + 2k_L + i\eta\omega_D) + F_2 k_L^2}{(-m\omega_D^2 + 2k_L + i\eta\omega_D)^2 - k_L^2}$$

$$A_2 = \frac{F_1 k_L^2 + F_2 k_L(-m\omega_D^2 + 2k_L + i\eta\omega_D)}{(-m\omega_D^2 + 2k_L + i\eta\omega_D)^2 - k_L^2} \tag{27}$$

We apply $k_L = k_1$. Using the complex amplitude (A_1 and A_2) and the linearized eigenstates of $\left(E_1 = \frac{1}{\sqrt{2}}\binom{1}{1} \text{ and } E_2 = \frac{1}{\sqrt{2}}\binom{1}{-1}\right)$, we can express the displacement field of the granules through the superposition of the states' coefficients α and β,

$$\vec{U} = \binom{u_1}{u_2} = \binom{A_1}{A_2} e^{i\omega_D t} = \frac{1}{\sqrt{|\tilde{\alpha}|^2 + |\tilde{\beta}|^2}} (\tilde{\alpha}|E_1\rangle + \tilde{\beta}|E_2\rangle) e^{i\omega_D t}$$

$$= (\alpha|E_1\rangle + \beta|E_2\rangle) e^{i\omega_D t} \tag{28}$$

$$\Rightarrow \begin{pmatrix} A_1 \\ A_2 \end{pmatrix} = \frac{1}{\sqrt{2}} \begin{pmatrix} \alpha + \beta \\ \alpha - \beta \end{pmatrix}$$

Substituting the complex amplitude (A_1 and A_2), we obtain the superposition of states coefficient α and β:

$$\alpha = \frac{A_1 + A_2}{\sqrt{2}} = \frac{k_L(F_1 + F_2)}{\sqrt{2}(-m\omega_D^2 + k_L + i\eta\omega_D)}$$

$$\beta = \frac{A_1 - A_2}{\sqrt{2}} = \frac{k_L(F_1 - F_2)}{\sqrt{2}(-m\omega_D^2 + 3k_L + i\eta\omega_D)} \tag{29}$$

4.4. Bloch States and 3D representations of the Superposition of States:

With the two possible forms of eigenmode vibration (E_1 and E_2), the displacement field vector $\vec{U}$ of the coupled granules, utilizing the coefficient of the complex amplitude can be expressed as follows:

$$\vec{U} = \alpha|E_1\rangle + \beta|E_2\rangle$$

$$\Rightarrow \vec{U} = r_\alpha e^{i\xi_\alpha}|E_1\rangle + r_\beta e^{i\xi_\beta}|E_2\rangle \tag{30}$$

where r_α and r_β are the magnitudes of the complex amplitude coefficients of α and β respectively. These states are represented in polar space as $r_\alpha = \cos\theta$ and $r_\beta = \sin\theta$, where θ is the polar angle, indicating the angle of superposition states with the z-axis of a Bloch sphere as shown in **Figure 5** [32, 60].

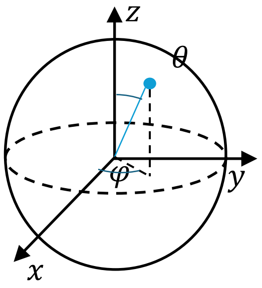

Figure 5: Three-dimensional illustration of the Bloch sphere, showcasing its relationship with the Cartesian coordinate system. This diagram highlights the sphere's axes and the defining angles—theta (θ) and phi (φ)-- representing an elastic bit's state.

In **Figure 5**, the z axis in a Bloch sphere represents the pure states $|E_1\rangle$ and $|E_2\rangle$, referred to as the polar angle. Multiplying both sides of Eq. (30) by the global phase $e^{-i\xi_\alpha}$ allows us to represent the displacement field as $\vec{U}' = e^{-i\xi_\alpha}\vec{U}$. The state space of the granular system can then be represented accordingly,

$$\vec{U}' = r_\alpha|E_1\rangle + r_\beta e^{i(\xi_\beta - \xi_\alpha)}|E_2\rangle$$

$$\vec{U}' = \cos\theta\,|E_1\rangle + \sin\theta\, e^{i\varphi}|E_2\rangle \tag{31}$$

Here, the phase difference between the complex amplitude coefficients is referred to as the azimuthal angle $\varphi = \xi_\alpha - \xi_\beta$, which signifies the rotation of the states in the x-y plane as depicted in **Figure 5**. To limit the ranges of both angles, we use a half-angle of polar angle θ to represent the state on the Bloch sphere. Since the global phase does not alter the superposition of states, we can determine the displacement field as,

$$\vec{U} = \cos\frac{\theta}{2}|E_1\rangle + e^{i\varphi}\sin\frac{\theta}{2}|E_2\rangle$$

$$\text{Where, } 0 \leq \theta \leq \pi \text{ and } 0 \leq \varphi \leq 2\pi \tag{32}$$

By the linear combination of E_1 and E_2 in Eq. (32), we can express the displacement field vector in terms of Bloch sphere angle θ and φ. The modal contribution of the displacement vector $\vec{U}$ is described in a column state vector $|\psi\rangle$ either through the superposition coefficients α and β or the Bloch sphere angles θ and φ.

$$|\psi\rangle = \binom{\alpha}{\beta} = \begin{pmatrix} \cos\frac{\theta}{2} \\ e^{i\varphi}\sin\frac{\theta}{2} \end{pmatrix} \tag{33}$$

The time dependency of the polar (θ) and azimuthal (φ) angle is based on the nonlinearity of the system. If we consider a linearized system based on the zeroth order amplitude of the granules $A_{1,0}$ and $A_{2,0}$, the Bloch states will be time-independent. Time dependency occurs when the system is nonlinear. In the later section, we will show both the time-dependent and independent Bloch states.

$$|\psi\rangle = \begin{pmatrix} \cos\frac{\tilde{\theta}(t)}{2} \\ e^{i\tilde{\varphi}(t)}\sin\frac{\tilde{\theta}(t)}{2} \end{pmatrix} \tag{34}$$

where

$$\tilde{\theta}(t) = 2\cos^{-1}(|\tilde{\alpha}(t)|)\,, \tilde{\varphi}(t) = \arg\big(\tilde{\alpha}(t)\big) - \arg\Big(\tilde{\beta}(t)\Big).$$

These angles, $\tilde{\theta}(t)$ and $\tilde{\varphi}(t)$, describe the superposition of the two eigenmodes E_1 and E_2 as a time-dependent combination. Hence, the polar angle $\tilde{\theta}(t)$ represents the relative magnitude of the eigenmodes, and the azimuthal angle $\tilde{\varphi}(t)$ encodes the phase difference between them. Hence, the Bloch sphere will provide a geometric representation of the elastic bit state space, with the north and south poles corresponding to the pure states $|E_1\rangle$ and $|E_2\rangle$, respectively. Any other point on the sphere will represent a superposition of these two states. The evolution of these angles on the Bloch sphere will reveal the underlying dynamics of the elastic bit's state, showing periodic oscillations that mirror the quantum behavior of a qubit under external influence.

5. EXPERIMENTAL PROCEDURE

We develop an experimental setup to observe the evolution of Bloch states and the accumulation of the Berry phase. **Figure 6** illustrates a driven nonlinear granular network that creates an elastic bit.

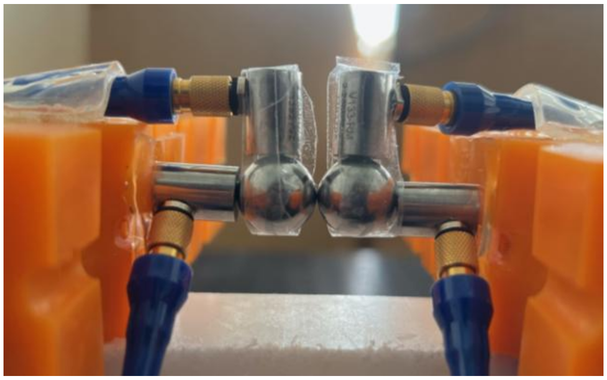

Figure 6: Experimental setup of the nonlinear granular network. One of the granules is driven by an ultrasonic transducer. Meanwhile, the lateral transducers record the responses of the vibrating granules.

The elastic granular beads in the experimental setup depicted in **Figure 6** are driven harmonically. Precompression is applied by the soft plastic material, which functions as a vise jaw and lessens vibrational transmission. At a fixed voltage amplitude of $120V_{p-p}$, the external driving frequency (ω_D) is swept from a lower value of 2 kHz to a higher value of 8 kHz with an increment of $100\,Hz$. Adaptable to varying frequencies and amplitudes are the nonlinear granular beads (52100 Alloy Steel: McMaster-Carr 9528K33, 1-inch diameter, Young's modulus $210\,GPa$, density $7810\ kg/m3$). One transducer (V133-RM Olympus IMS) at one end of the system drives it. An amplifier (PD200, 60W high-bandwidth, low-noise linear amplifier) and a waveform generator (B&K Precision 4055B) are used to drive the transducer. Responses are recorded using three comparable transducers. Record transducers are positioned with one in the longitudinal direction and two in the lateral direction. To reduce recording errors, the signal responses from the three recording transducers are averaged over 512 time series using a Tektronix MDO3024 Mixed Domain Oscilloscope. Custom algorithms based on MATLAB are used to control and process the generation of signals with different frequencies and amplitudes, as well as the recording and processing of these signals and data. A bench vise is used to fix the initial displacement, δ_0, between the centers of the granules and provide a uniform compression force, F_0, at both ends of the system. At a steady state, the granules' lateral detecting transducers provide the responses. To the best of human vision, the granules are guaranteed to be center-to-center aligned. The natural frequency of the vise holding the setup can cause mechanical disturbance in the system. We filtered the data using a low pass frequency of $175\ kHz$ in order to account for environmental noises after processing the data for the sampling frequency of $999.89\ kHz$. To obtain the signal data's pure response, the resulting signal is processed up to $25\ kHz$. This can be used to determine the signal-to-noise ratio (SNR) of the existing system. One metric for assessing a signal's quality in the presence of noise is the signal-to-noise ratio (SNR). It stands for the power ratio of the signal to the noise in acoustics.

6. THEORETICAL AND EXPERIMENTAL DEMONSTRATION OF CLASSICAL ANALOGOUS QUANTUM SUPERPOSITION OF STATES AND THE QUANTUM ANALOGOUS LOGIC GATE

Through the operation of the system, we can observe the formation of elastic bits. Here, we will explore how to control the superposition of states in the theoretical formation of elastic bits. Later, we will show the comparison of the theoretical and experimental formation of the time-dependent superposition of states in a nonlinear granular network.

6.1. Theoretical Control of the Superposition of States in Linearized Network:

To investigate these aspects, we apply an external harmonic excitation, driving both granules with differing force amplitudes. The driving force takes the form:

$$F_1 = \mathcal{E} + (1-\mathcal{E})e^{i\xi}, \qquad F_2 = \mathcal{E} - (1-\mathcal{E})e^{i\xi}. \tag{35}$$

Equation (32) shows how the system is driven so that the ratio of the two pure states $(\mathcal{E})$ of the linearized granular system and their phase difference (ξ) determine the amplitudes of the external forces. External signal generators can be used in experiments to change these parameters. We will demonstrate how different superpositions of the $|E_1\rangle$ and $|E_2\rangle$ states can be obtained by adding the drivers' frequency and amplitudes F_1 and F_2. We will then be able to look at their state vectors on the Bloch sphere. Therefore, we will show that despite system (13) being homogeneous.

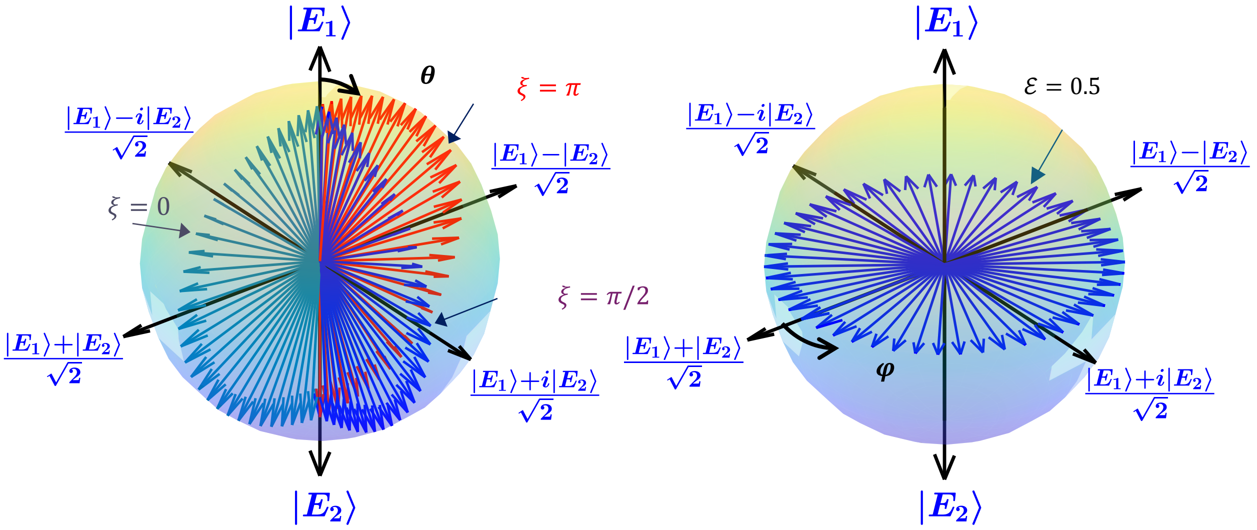

Figure 7: Illustration of the transformation of states of the two-level elastic bit system, represented geometrically on the Bloch sphere. Panel (a) shows the variation of the polar angle (θ) with the ratio of $\mathcal{E}$ while keeping the azimuthal angle (φ) constant, illustrating the transition from pure states E_1 $(\theta = 0)$ to E_2 $(\theta = \pi)$ and various superpositions in between. The initial phase ξ was fixed during this demonstration. Panel (b) focuses on the azimuthal angle (φ) while keeping θ constant, by varying ξ from $-\pi$ to $+\pi$ for a set value of $\mathcal{E} = 0.5$. The arrows on the sphere indicate the direction of state vector evolution for different parameter adjustments, thereby providing a clear visual guide to understanding how external parameters like $\mathcal{E}$ and ξ influence the states of the elastic bit. System parameters: $m = 1, k_L = 1, \eta = 0.003, \omega_D = \sqrt{2}$. All the parameters used in this study are non-dimensional. We use a small damping in the system to represent that the system preserves its oscillatory behavior due to external excitation and remains susceptible to the change of the external excitation.

To investigate the behavior of the elastic bit on the Bloch sphere, we adjust the parameters $\mathcal{E}$ and ξ as described in Eq. (35). **Figure 7** shows how these changes affect the polar angle (θ) and azimuthal angle (φ). We can visually trace the evolution of these angles onto the Bloch sphere. This visualization demonstrates how varying $\mathcal{E}$ and ξ influences the superposition states of the elastic bit. Specifically, it reveals the range and nature of superposition states achievable through parameter manipulation. The Bloch sphere thus serves as a valuable tool for comprehending how different parameters alter the system's states.

To investigate scenarios where the azimuthal angle φ remains constant while the polar angle θ varies, we keep ξ fixed and adjust the ratio of $\mathcal{E}$. At $\theta = 0$, a pure state of E_1 is achieved, and at $\theta = \pi$, a pure state of E_2 is obtained (see **Figure 7a**). As θ changes from 0 to π (**Figure 7a**), it signifies the generation of any superposition of states, incorporating both pure states E_1 and E_2. The superpositions $\left(\frac{|E_1\rangle+|E_2\rangle}{\sqrt{2}}\right)$ and $\left(\frac{|E_1\rangle+i|E_2\rangle}{\sqrt{2}}\right)$ are realized when the initial phase ξ is 0 and $\pi/2$, respectively. And the superposition of $\left(\frac{|E_1\rangle-|E_2\rangle}{\sqrt{2}}\right)$ are observed in the case of $\xi = \pi$.

We then explore another scenario where θ is fixed, and φ varies, achieved by different parameter adjustments. As demonstrated in **Figure 7b**, by setting $\mathcal{E}$ to 0.5 and varying ξ from $-\pi$ to $+\pi$, we observe a constant θ while φ completes a full 2π rotation.

6.2. Quantum Analogous Logic Gate:

Following the detailed illustration of a two-level elastic bit on a Bloch sphere, we concentrate on using and modifying these representations in real-world scenarios. Revisiting **Figure 7a**, we noticed that the pure states E_1 and E_2 manifest under different driving parameters. Equation (33) reveals that these pure states occur at polar angles θ of 0 and π, respectively, while the azimuthal angle φ indicates the phase difference between E_1 and E_2. Further, the equal superpositions of states, $\left(\frac{|E_1\rangle+|E_2\rangle}{\sqrt{2}}\right)$ and $\left(\frac{|E_1\rangle+i|E_2\rangle}{\sqrt{2}}\right)$, are represented on the Bloch sphere at coordinates (θ,φ) = $(\pi/2, 0)$ and $(\pi/2, \pi/2)$, and the opposite of these states are represented by $\left(\frac{|E_1\rangle-|E_2\rangle}{\sqrt{2}}\right)$ and $\left(\frac{|E_1\rangle-i|E_2\rangle}{\sqrt{2}}\right)$ located at (θ,φ) = $(\pi/2,0)$ and $(\pi/2,2\pi/3)$. These superposed states are achieved through combinations of $\mathcal{E}$ and ξ, induced by external excitations. In order to show the convertibility to superposed states and the manipulation of these states on the Bloch sphere with an elastic bit, this section describes how these states change and shows the use of several quantum-analogous logical gates. Like the classical logic gates found in conventional computers, the logic gates are crucial to quantum-analogue computing. They are unitary operators that use the concepts of superposition and entanglement to permit state changes, which are essential for the operation of algorithms inspired by quantum mechanics [61]. Here we demonstrate the quantum analogous gate in the elastic bit and their corresponding unitary transformation matrix, which has basis state of $E_1 = \frac{1}{\sqrt{2}}\begin{pmatrix}1\\1\end{pmatrix}$ and $E_2 = \frac{1}{\sqrt{2}}\begin{pmatrix}1\\-1\end{pmatrix}$.

In **Figure 8**, we illustrate the transformations of elastic bit states through quantum-analogue gate operations as follows: (i) from one pure state to another (**Figure 8a-b**), (ii) from a pure state to a superposition of states, or vice versa (**Figure 8c**), and (iii) from one superposition of states to another (**Figure 8d-f**). Specifically, the Pauli X gate (**Figure 8a**) converts the state $|E_1\rangle$ to $|E_2\rangle$ and vice versa, representing a bit flip in the quantum analogue system. In contrast, the Pauli Y gate (**Figure 8b**) transforms $|E_1\rangle$ to $i|E_2\rangle$ and $|E_2\rangle$ to $-i|E_1\rangle$, and vice versa. This indicates that the Pauli X and Y gates alter the state $|E_1\rangle$ to $|E_2\rangle$ along different trajectories, signifying distinct operational paths. The corresponding transformation matrices for these state changes are:

$$\begin{bmatrix} 1 & 0 \\ 0 & -1 \end{bmatrix} |E_1\rangle = |E_2\rangle \text{ and } \begin{bmatrix} 1 & 0 \\ 0 & -1 \end{bmatrix} |E_2\rangle = |E_1\rangle,$$

$$\begin{bmatrix} 0 & i \\ -i & 0 \end{bmatrix} |E_1\rangle = i|E_2\rangle \text{ and } \begin{bmatrix} 0 & i \\ -i & 0 \end{bmatrix} |E_2\rangle = -i|E_1\rangle.$$

The unitary operation, represented by the matrix $\begin{bmatrix} 1 & 0 \\ 0 & -1 \end{bmatrix}$, serves as the quantum-analogue counterpart to the classical NOT gate, commonly known as the Pauli X gate in quantum computing. Unlike the transformation matrix $\begin{bmatrix} 0 & 1 \\ 1 & 0 \end{bmatrix}$ used in quantum mechanics, our analogous system employs a different matrix. This change arises because the computational bases in a true quantum system are $|0\rangle = \begin{pmatrix} 1 \\ 0 \end{pmatrix}$ and $|1\rangle = \begin{pmatrix} 0 \\ 1 \end{pmatrix}$. However, in our elastic bit system, we have defined the bases as $|E_1\rangle = \frac{1}{\sqrt{2}}\begin{pmatrix} 1 \\ 1 \end{pmatrix}$ and $|E_2\rangle = \frac{1}{\sqrt{2}}\begin{pmatrix} 1 \\ -1 \end{pmatrix}$. Furthermore, within the $|E_1\rangle$ and $|E_2\rangle$ bases, the Pauli Y matrix is denoted by $\begin{bmatrix} 0 & i \\ -i & 0 \end{bmatrix}$. The Hadamard gate, as illustrated in Fig. 3c, transforms the pure states. Specifically, it maps $|E_1\rangle$ to $\left(\frac{|E_1\rangle+|E_2\rangle}{\sqrt{2}}\right)$ and $|E_2\rangle$ to $\left(\frac{|E_1\rangle-|E_2\rangle}{\sqrt{2}}\right)$. This transformation signifies the mapping of a pure state to a linear combination of superposed states, and vice versa, through the Hadamard matrix $\frac{1}{\sqrt{2}}\begin{bmatrix} 1 & 1 \\ 1 & -1 \end{bmatrix}$ as follows:

$$\frac{1}{\sqrt{2}}\begin{bmatrix} 1 & 1 \\ 1 & -1 \end{bmatrix} |E_1\rangle = \left(\frac{|E_1\rangle + |E_2\rangle}{\sqrt{2}}\right); \frac{1}{\sqrt{2}}\begin{bmatrix} 1 & 1 \\ 1 & -1 \end{bmatrix} |E_2\rangle = \left(\frac{|E_1\rangle - |E_2\rangle}{\sqrt{2}}\right).$$

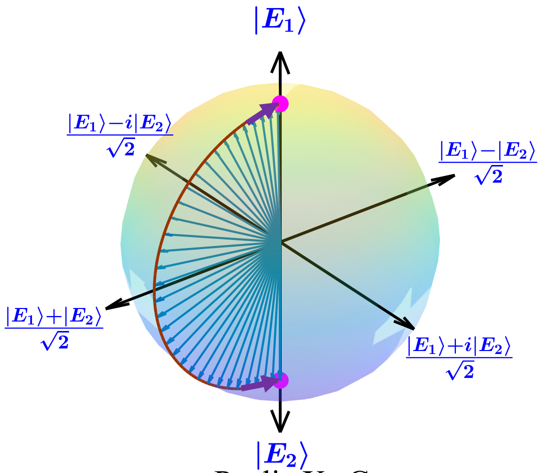

Pauli X Gate:

$[1 \quad 0]$

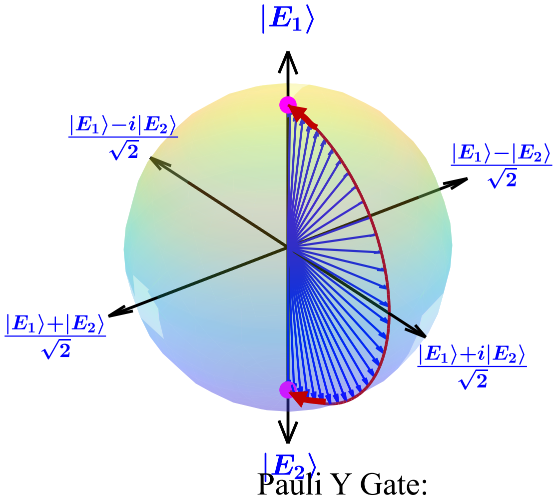

Pauli Y Gate:

$[0 \quad i]$

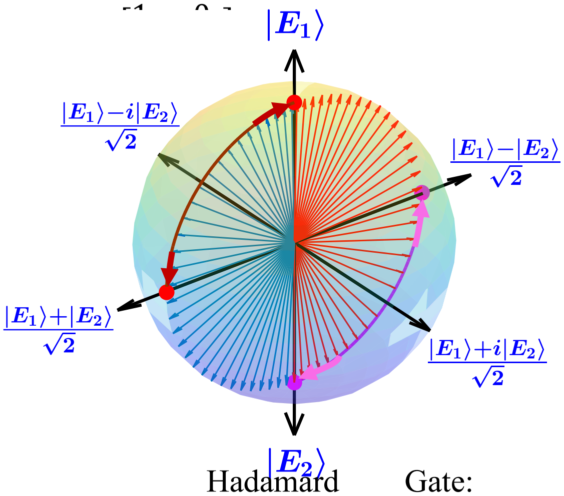

Hadamard Gate:

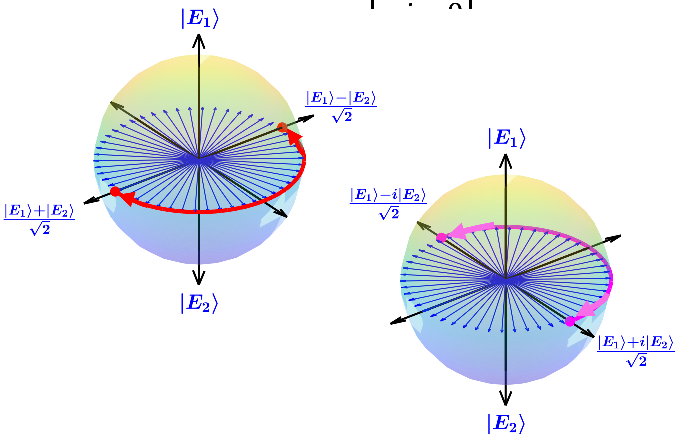

Pauli Z Gate: $\begin{bmatrix}0 & 1\\ 1 & 0\end{bmatrix}$

$1 \; [1 \quad 1]$

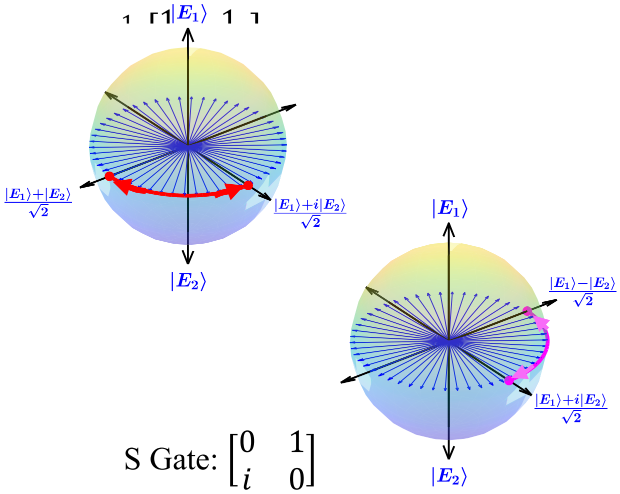

S Gate: $\begin{bmatrix}0 & 1\\ i & 0\end{bmatrix}$

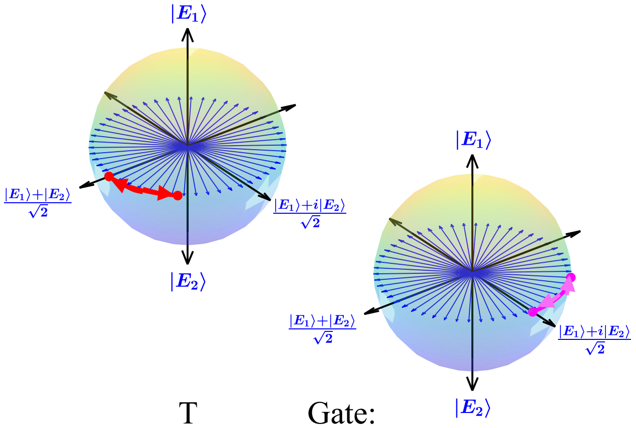

T Gate:

$[0 \quad 1]$

Figure 8: Transformation of the elastic bit states through various quantum-analogue logical gates. Each panel represents a different type of gate operation: Panels (a) and (b) display the effects of the Pauli X and Y gates, respectively, showcasing state conversions ($|E_1\rangle$ to $|E_2\rangle$ and vice versa) along distinct operational paths. Panel (c) depicts the Hadamard gate's role in mapping pure states to equal superpositions and conversely. Panels (d), (e), and (f) focus on the phase shift gate families, Pauli Z, S, and T gates, respectively. These gates demonstrate the transformation of superposed states by altering only one aspect of the complex amplitude's coefficient, thus modifying the state's direction through the azimuthal angle φ. The specific transformations effected by each gate are represented through transitions on the Bloch sphere, with arrows indicating the direction and nature of state changes. System parameters: $m = 1, k_L = 1, \eta = 0.003, \omega_D = \sqrt{2}$.

The Pauli Z, S, and T gates (demonstrated in **Figure 8d-f**) are instrumental in transitioning from one superposed state to another. These gates modify only one aspect of the complex amplitude's coefficient: they alter the state's direction through the azimuthal angle φ by π, $\pi/2$, and $\pi/4$, respectively. The Pauli Z gate, often referred to as a phase flip, uniquely affects the linear equal superposition of states. While it leaves $|E_1\rangle$ and $|E_2\rangle$ states unchanged, it transforms the state $\left(\frac{|E_1\rangle+|E_2\rangle}{\sqrt{2}}\right)$ into $\left(\frac{|E_1\rangle-|E_2\rangle}{\sqrt{2}}\right)$ and $\left(\frac{|E_1\rangle+i|E_2\rangle}{\sqrt{2}}\right)$ to $\left(\frac{|E_1\rangle-i|E_2\rangle}{\sqrt{2}}\right)$ and vice versa, as can be seen through the following transformation matrix $\begin{bmatrix} 0 & 1 \\ 1 & 0 \end{bmatrix}$ (refer to **Figure 8d**):

$$\begin{bmatrix} 0 & 1 \\ 1 & 0 \end{bmatrix}\left(\frac{|E_1\rangle + |E_2\rangle}{\sqrt{2}}\right) = \left(\frac{|E_1\rangle - |E_2\rangle}{\sqrt{2}}\right),$$

$$\begin{bmatrix} 0 & 1 \\ 1 & 0 \end{bmatrix}\left(\frac{|E_1\rangle + i|E_2\rangle}{\sqrt{2}}\right) = \left(\frac{|E_1\rangle - i|E_2\rangle}{\sqrt{2}}\right).$$

The other set of gates, as shown in **Figure 8e** and **Figure 8f**, belong to the phase shift gates family. These gates function by mapping the superposition of states. Specifically, they map the state $\left(\frac{|E_1\rangle+|E_2\rangle}{\sqrt{2}}\right)$ to $e^{i\varrho}\left(\frac{|E_1\rangle+|E_2\rangle}{\sqrt{2}}\right)$, and the state $\left(\frac{|E_1\rangle+i|E_2\rangle}{\sqrt{2}}\right)$ to $e^{i\varrho}\left(\frac{|E_1\rangle+i|E_2\rangle}{\sqrt{2}}\right)$, where ϱ represents the phase shift. And the same goes for their opposite counterparts. For the S gate (**Figure 8e**), ϱ equals $\pi/2$, and for the T gate (**Figure 8f**), it equals $\pi/4$. The operations of these gates are as follows:

$$\begin{bmatrix} 0 & 1 \\ i & 0 \end{bmatrix}\left(\frac{|E_1\rangle+|E_2\rangle}{\sqrt{2}}\right) = e^{\frac{i\pi}{2}}\left(\frac{|E_1\rangle+|E_2\rangle}{\sqrt{2}}\right); \begin{bmatrix} 0 & 1 \\ i & 0 \end{bmatrix}\left(\frac{|E_1\rangle+i|E_2\rangle}{\sqrt{2}}\right) = e^{\frac{i\pi}{2}}\left(\frac{|E_1\rangle+i|E_2\rangle}{\sqrt{2}}\right).$$

$$\begin{bmatrix} 0 & 1 \\ e^{\frac{i\pi}{4}} & 0 \end{bmatrix}\left(\frac{|E_1\rangle+|E_2\rangle}{\sqrt{2}}\right) = e^{\frac{i\pi}{4}}\left(\frac{|E_1\rangle+|E_2\rangle}{\sqrt{2}}\right); \begin{bmatrix} 0 & 1 \\ e^{\frac{i\pi}{4}} & 0 \end{bmatrix}\left(\frac{|E_1\rangle+i|E_2\rangle}{\sqrt{2}}\right) = e^{\frac{i\pi}{4}}\left(\frac{|E_1\rangle+i|E_2\rangle}{\sqrt{2}}\right).$$

The transformation matrix operation, which changes one state into another, is used to illustrate the elastic bit's quantum analogous gate operation in this section. We demonstrate these states using the Bloch spheres in previous section. In order to change states, we evolve the initial phase ξ and the state ratio $\mathcal{E}$. Therefore, comparable state transformation can be accomplished by both the external excitation manipulation and the quantum gate operation. Using gate operations, we demonstrate that our elastic bit, which is created by the linearized granular network, adheres to the quantum analogous interpretation.

6.3. Manipulating the State Evolution in Nonlinear Network:

From Eq. (34) we observe that the polar $\tilde{\theta}(t)$ and the azimuthal $\tilde{\varphi}(t)$ angles depend on the complex coefficients $\tilde{\alpha}(t)$ and $\tilde{\beta}(t)$, which are themselves influenced by the external driving forces, frequency, and static precompression. Hence, the evolution of the elastic bit's state is governed by the external driving parameters, including the amplitudes F_1 and F_2, the frequency

ω_D, and the static precompression δ_0. By adjusting these parameters, we can control the path the elastic bit takes on the Bloch sphere. Figure 1 illustrates this by showing the evolution of the elastic bit's state for different driving conditions. The external drivers influence both the polar and azimuthal angles, and variations in these parameters lead to different trajectories on the Bloch sphere.

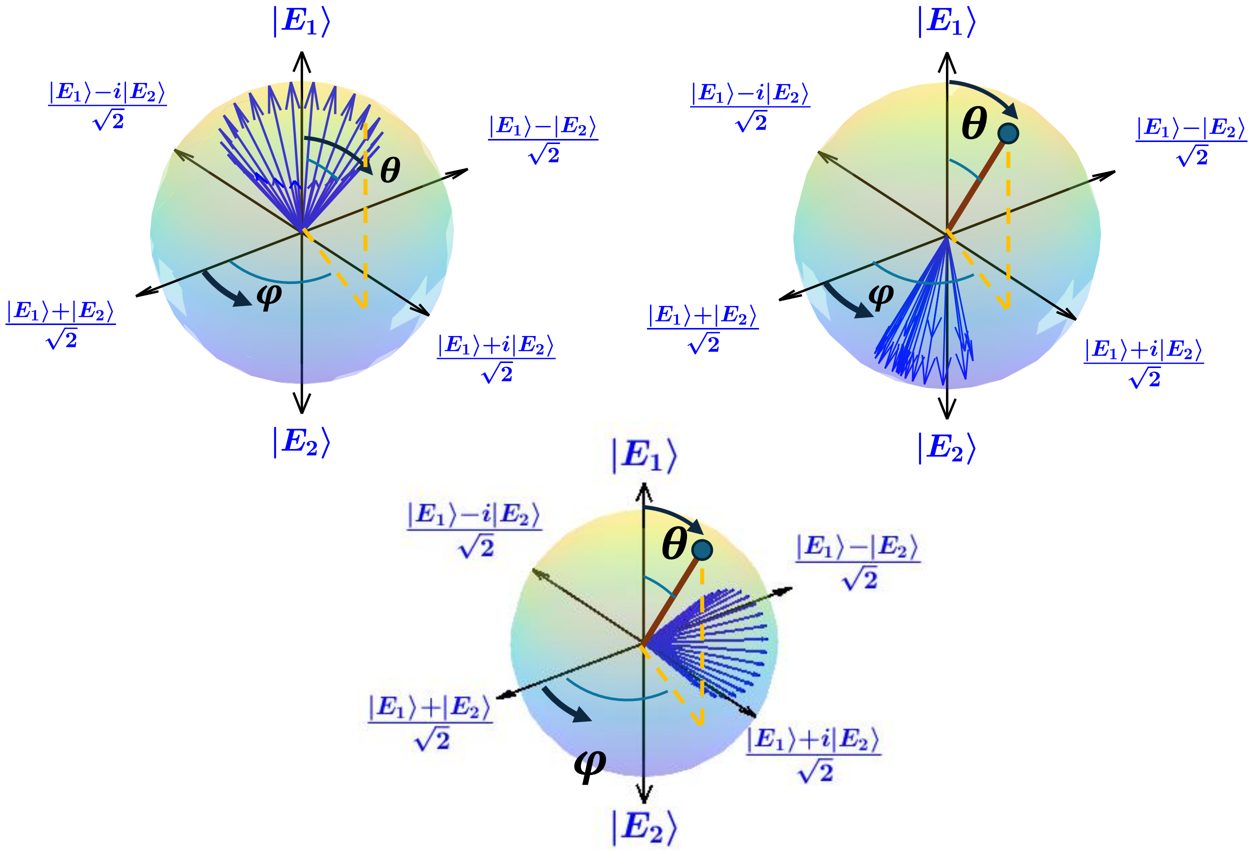

Figure 9: Time-Dependent State Evolution of Elastic Bits. The time-dependent evolution of the elastic bit's state, represented on the Bloch sphere, under a specific set of driving frequencies and amplitudes, highlighting the continuous loop and periodic return to the initial state. The polar angle $\tilde{\theta}(t)$ remained nearly constant, indicating that the system's evolution occurred predominantly

along the equator of the sphere. Panels (a) to (c) show the effects of varying external stimuli like frequency on the system's varying state evolutions.

Figure 9 shows that the azimuthal angle $\tilde{\varphi}$ makes a complete 2π revolution in one full period. In contrast, the polar angle $\tilde{\theta}(t)$ variation is negligible, indicating that the state primarily evolves around the equator of the Bloch sphere. As a result, the state of the elastic bit evolves continuously over time. This means that the state vector undergoes periodic motion along the surface of the Bloch sphere, returning to its initial state after each cycle. Here, time permits the parametric exploration of paths on the Bloch sphere without the need to change the external drivers' parameters. In contrast, our previous work has shown the time-independent evolution of the elastic bit states by adjusting the external driver parameters.

Furthermore, **Figure 9** illustrates that different evolutions of the states on the Bloch sphere can be achieved by varying external parameters. In **Figure 9**, we present three cases in which the elastic bit undergoes rotations around different axes on the Bloch sphere; however, after a certain duration or angle, the state vector returns to its original position. This periodicity is essential for the calculation of the Berry phase, a topological quantity that characterizes the evolution of the state vector over time.

6.4. Time Response in Granular System Setup:

We tune peak-to-peak voltage to fix the amplitudes of external excitations to experimentally observe different nonlinear responses in such a damped-driven, essentially nonlinear granular system. However, the external driver's frequency (ω_D) fluctuates between $100\ Hz$ and $20\ kHz$ in increments of $10\ Hz$, with a resting period to achieve a steady state. We experimentally obtain **Figure 10a**, which displays the time series of the transmission amplitudes recorded by the detecting transducers of each granule at a steady state, for various combinations of driving conditions (frequency and amplitude). The Fourier sum of the linear and nonlinear modes, each with a distinctive frequency, makes up the transmission amplitude field shown in **Figure 10a**. The temporal Fourier transform (fft) of the granule's amplitude in **Figure 10b** makes this clear. We set a threshold of 1% of the maximum amplitude to remove noise and identify the system's dominant characteristic frequencies. For every dominant characteristic frequency, we also compute the phase difference between the granules. For instance, we can observe in the left panel of **Figure 10c** that the phase difference between granules is nearly zero for the driving frequency, which is $\omega = \omega_D = 9.55\ kHz$, the lowest dominant characteristic frequency. This suggests that the amplitude field of the granules' system can be described by the state, $E_1 = \frac{1}{\sqrt{2}}\begin{pmatrix}1\\1\end{pmatrix}$ at the characteristic frequency $\omega = \omega_D = 9.55\ kHz$. Conversely, if we alter the driving frequency to, $\omega_D = 5.3\ kHz$, we can see that the phase difference between the granules is near π at the lowest dominant characteristic frequency, $\omega = \omega_D = 5.3\ kHz$, in the right panel of Fig. 1c. The amplitude field at this characteristic frequency can therefore be described by the following state: $E_2 = \frac{1}{\sqrt{2}}\begin{pmatrix}1\\-1\end{pmatrix}$ Next, we see in the left and right panels of **Figure 10c** that the phase difference between granules is neither 0 nor π at the second and third higher harmonics, $2\omega_D$ and $3\omega_D$. Therefore, the states can be described by a combination of, E_1 and E_2.

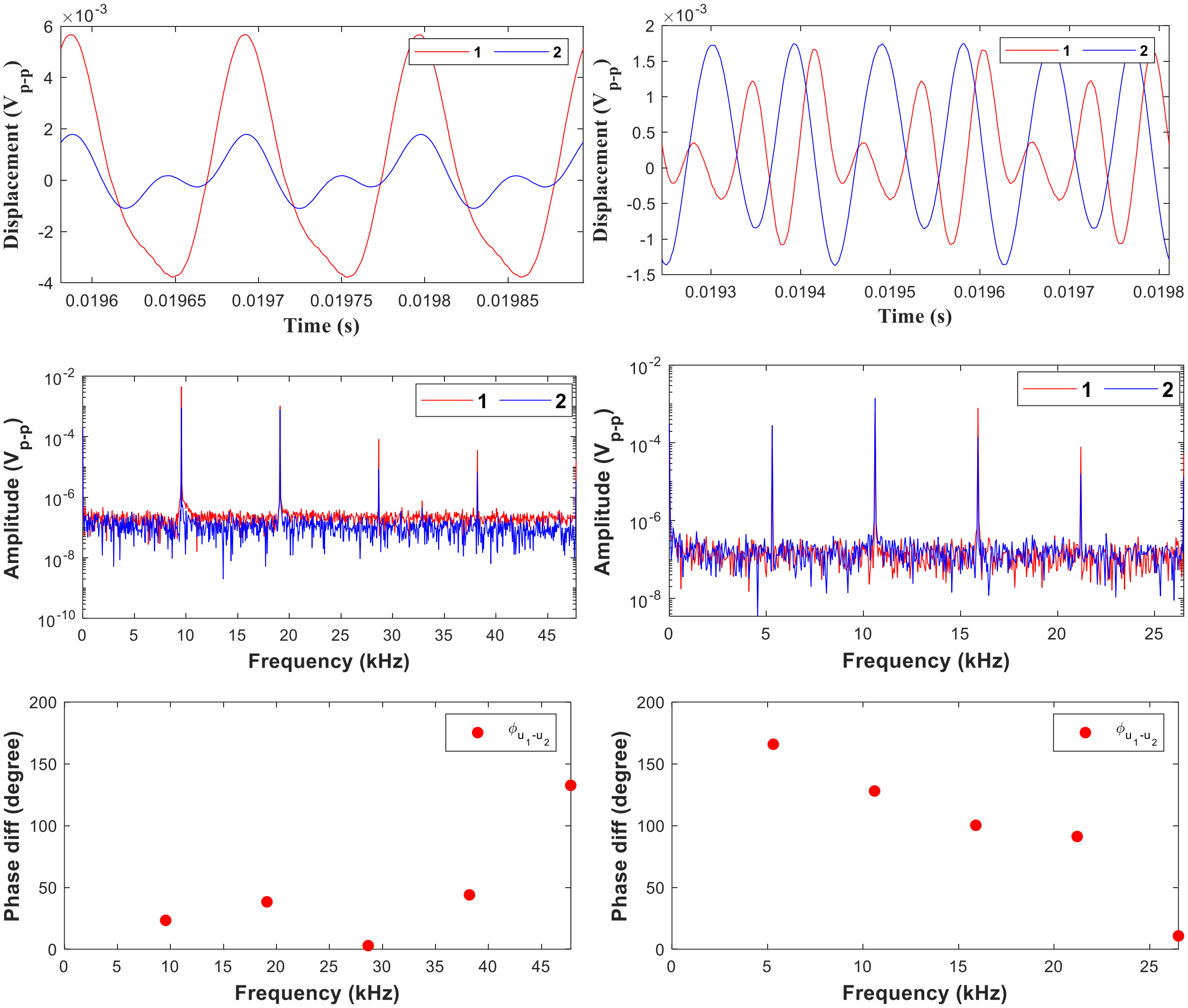

Figure 10: Time Response of two granular network due to different driving frequencies. (a) Amplitude versus time recorded by the detecting transducers of each granule at steady state, revealing rich nonlinear responses of the system. Left panel: driving frequency $\omega_D = 9.55$ kHz and driving amplitude 100 V_{p-p}; Right panel: driving frequency $\omega_D = 5.3$ kHz and driving amplitude 100 V_{p-p}. **(b)** Temporal Fourier transform of the granules amplitudes, and **(c)** phase differences between granules; revealing the combinations of E_1 and E_2 eigenstates associated with each characteristic frequency.

6.5. Classical Analogous Superposition of States of Nonlinear Network:

To experimentally create an elastic bit in a classical nonlinear granular system that can generate a time-dependent superposition of states, we utilize a setup similar to that described in Ref. [48]. It is known that the nonlinearity of the granular system can be controlled by adjusting external driving parameters such as frequency, amplitude, or static precompression [18]. In our theoretical analysis, as shown in Eq. (34), we demonstrate that when the two granules are subjected to static precompression and driven at a specific frequency, the nonlinear vibrational mode can be expressed in a linear normal mode orthonormal basis (E_1 and E_2) with time-dependent Bloch states ($\tilde{\theta}(t)$ and $\tilde{\varphi}(t)$). These Bloch states constitute the components of a state vector in the two-dimensional Hilbert space of the elastic bit, allowing the system to explore this space parametrically over time along closed periodic paths. Following these theoretical procedures, we use the same orthonormal basis of the elastic bit to map the experimental displacement fields to the Bloch states ($\tilde{\theta}$ and $\tilde{\varphi}$).

Following the theoretical modeling procedures, we used the same orthonormal basis of the elastic bit to map the experimental displacement fields to coherent states. This mapping enables us to track the evolution of the states through the Bloch states ($\tilde{\theta}$ and $\tilde{\varphi}$).

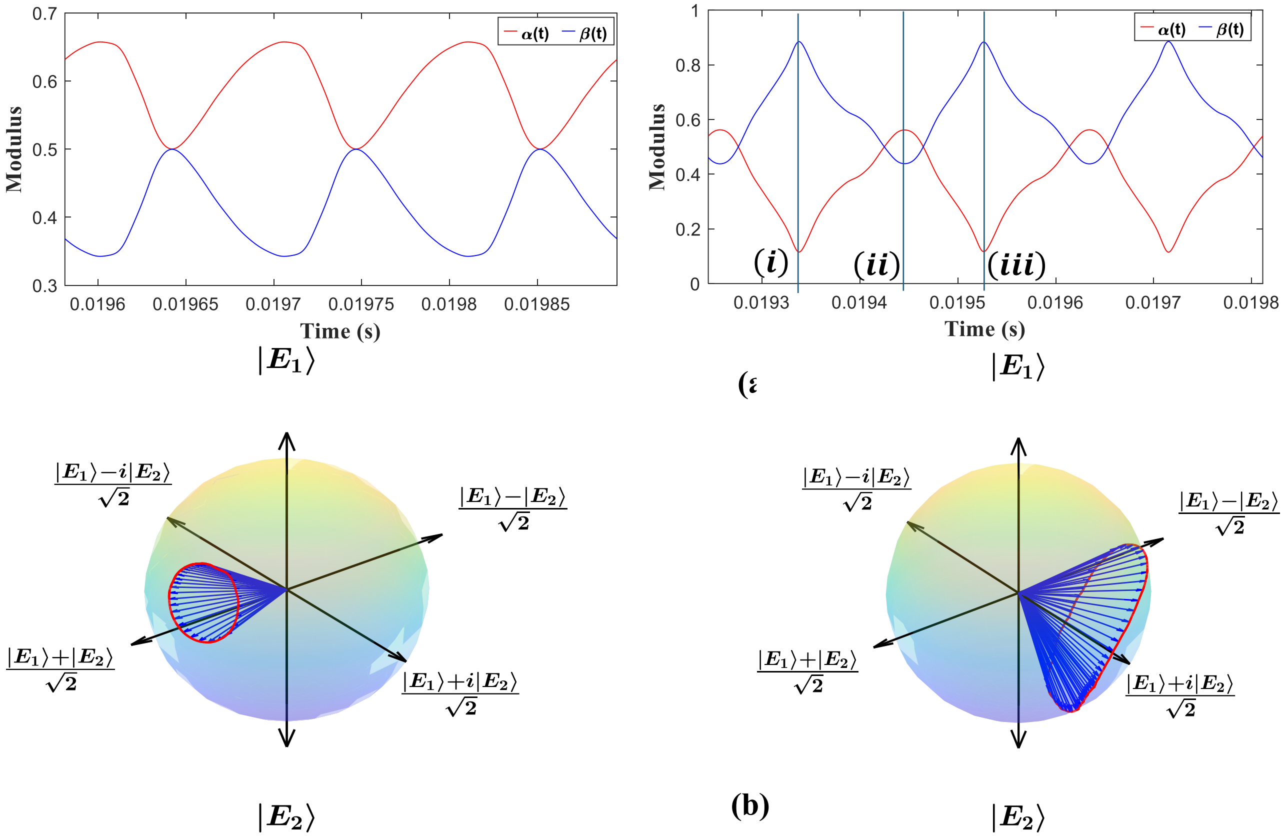

Figure 11: Experimental Manifestation of Elastic Bit Evolution. (a) Time evolution of the modules of the complex amplitudes, $\tilde{\alpha}(t)$ and $\tilde{\beta}(t)$, of two mutually orthogonal states $|E_1\rangle$ and $|E_2\rangle$. the vertical lines labeled (i), (ii), and (iii) correspond to three different time instants: $(i) = t_1, (ii) = t_2,$ and $(iii) = t_3,$ where $t_3 > t_2 > t_1$. (b) Trajectories on the Bloch Sphere: Cyclic evolution of the elastic bit's states on the Bloch sphere at various driving frequencies, illustrating the rotational paths traced by the system's state. The state follows distinct trajectories, highlighting the path dependence of the evolution. The amplitude of the external driver remains constant, while the frequency varies to affect the cyclic path.

From the fft plot of **Figure 11a** left panel, we see that the amplitude α_1 of frequency ω is the dominant term, and it corresponds to pure $|E_1\rangle$ eigenstate since at that frequency the phase difference is almost zero (cf. **Figure 10c** left panel). Hence, in Eq. (25), we expect that the coefficient $\tilde{\alpha}(t)$ will be dominant in comparison to the coefficient $\tilde{\beta}(t)$, as is also confirmed in **Figure 11a** left panel. **Figure 11a**, we observe the time dependencies of the modules of the complex amplitudes, $\tilde{\alpha}(t)$ and $\tilde{\beta}(t)$, of two mutually orthogonal states $|E_1\rangle$ and $|E_2\rangle$. Next, if we move to a different driving frequency, we observe from **Figure 11a** right panel that it is possible to vary the coefficients of the coherent superposition of states significantly. In **Figure 11a** right panel, we see that for the case of driving frequency $\omega = 5.3$ kHz, the coefficient $\tilde{\beta}(t)$ dominates, which can be inferred from the right panels of **Figure 10b-c** since E_2 eigenstate dominates at the first dominant characteristic frequency. Hence, the elastic bit states live in a 2D Hilbert space, and through the driving parameters, we can navigate the Hilbert space significantly. An elastic bit is, therefore, a classical analogue with respect to superposition of a qubit-the critical component of quantum computing platforms.

Figure 11b illustrates the experimental cyclic evolution of the elastic bit's states, represented as rotations on the Bloch sphere at different driving frequencies while keeping the amplitudes of the driver's constant. Compared to **Figure 9**, **Figure 11b** navigates a broader range of the Bloch sphere and creates twists within a single cyclic evolution. Additionally, **Figure 11**b displays distinct trajectories, likely due to the inclusion of higher-order harmonics beyond the third order in the theoretical calculations used for **Figure 9**. These higher harmonics introduce unique combinations of amplitude and phases, resulting in these unique trajectories.

6.6. Experimental realization of Hadamard gate

As seen in **Figure 11a**, time allows the system to tune the superposition of states created by the two eigenmodes. Hence, the passage of time is therefore equivalent to applying a unitary transformation to the superposed states. To illustrate this point, let us focus on time instant t_1 labeled (i) in **Figure 11a** right panel. For such an instant, using Eq. (26), the modal contribution in the mode superposition of the displacement state vector can be written as:

$$|\psi\rangle = \begin{pmatrix} \frac{1}{|\alpha_1|}\alpha_1 e^{i\omega_D t_1} + \frac{1}{\sqrt{|\alpha_2|^2+|\beta_2|^2}}\alpha_2 e^{i2\omega_D t_1} + \frac{1}{\sqrt{|\alpha_3|^2+|\beta_3|^2}}\alpha_3 e^{i3\omega_D t_1} \\ \frac{1}{|\beta_1|}\beta_1 e^{i\omega_D t_1} + \frac{1}{\sqrt{|\alpha_2|^2+|\beta_2|^2}}\beta_2 e^{i2\omega_D t_1} + \frac{1}{\sqrt{|\alpha_3|^2+|\beta_3|^2}}\beta_3 e^{i3\omega_D t_1} \end{pmatrix}. \tag{36}$$

However, in the above equation, $\alpha_1 \approx 0$, since the phase difference between granules is close to π at the lowest dominant characteristic frequency ω_D, as illustrated in **Figure 10c** right panel. Hence, at this characteristic frequency, the amplitude field can be described by the state: $E_2 = \frac{1}{\sqrt{2}}\begin{pmatrix} 1 \\ -1 \end{pmatrix}$. Therefore, the superposition of states can be written as:

$$\begin{aligned} \vec{U} &\equiv \begin{pmatrix} 0.0007 - 0.0193i \\ 0.7565 - 0.6538i \end{pmatrix} (|E_1\rangle + |E_2\rangle) \\ &\equiv \left(0.0194e^{-i\frac{\pi}{2}}\right)|E_1\rangle + \left(0.9998e^{-i\frac{\pi}{4}}\right)|E_2\rangle \\ &\equiv \cos\frac{\theta}{2}|E_1\rangle + e^{i\varphi}\sin\frac{\theta}{2}|E_2\rangle; \theta = \pi, \varphi = -\frac{\pi}{4} \end{aligned} \tag{37}$$

With an estimated uncertainty of $\frac{\pi}{20}$ in θ and $\frac{3\pi}{50}$ in φ, which depends on the amplitude threshold value used for selecting dominant characteristic frequencies (cf. **Figure 10b**). The state corresponds to time instant t_1 of Fig. 1d right panel (Eq. (7)) is also depicted in **Figure 12** on a Bloch sphere. A linear combination of the $|E_1\rangle$ and $|E_2\rangle$ states with complex coefficients is represented by a point on this sphere (**Figure 12a**). Similarly, the state corresponds to time instant t_2 of **Figure 11b** right panel (labeled (ii)) can also be written as:

$$\vec{U} \equiv \begin{pmatrix} 0.5354 - 0.476i \\ -0.5344 + 0.4486i \end{pmatrix} (|E_1\rangle + |E_2\rangle)$$

$$\equiv \left(0.716e^{-i\frac{\pi}{4}}\right) |E_1\rangle + \left(0.698e^{i\frac{3\pi}{4}}\right) |E_2\rangle$$

$$\equiv cos\frac{\theta}{2}|E_1\rangle + e^{i\varphi}\, sin\frac{\theta}{2}|E_2\rangle; \theta = \frac{\pi}{2}, \varphi = \pi \tag{38}$$

and the state is again represented in **Figure 12b** on a Bloch sphere. A Hadamard gate 'rotates' the initial state of Eq. (37) (labeled (i)), which is almost a pure state $|E_2\rangle$, to a superposition state of the form Eq. (38) (labeled (ii)) through the transformation:

$$\frac{1}{\sqrt{2}}\begin{pmatrix} 1 & 1 \\ 1 & -1 \end{pmatrix}\begin{pmatrix} 0.007 - 0.0193i \\ 0.7565 - 0.6538i \end{pmatrix} = \begin{pmatrix} 0.5354 - 0.476i \\ -0.5344 + 0.4486i \end{pmatrix} \tag{39}$$

The transformation matrix $\frac{1}{\sqrt{2}}\begin{pmatrix} 1 & 1 \\ 1 & -1 \end{pmatrix}$ is the usual Hadamard gate. If we apply the Hadamard gate on the state (ii), we return to the initial pure state $|E_2\rangle$ at time instant t_3 (labeled (iii)).

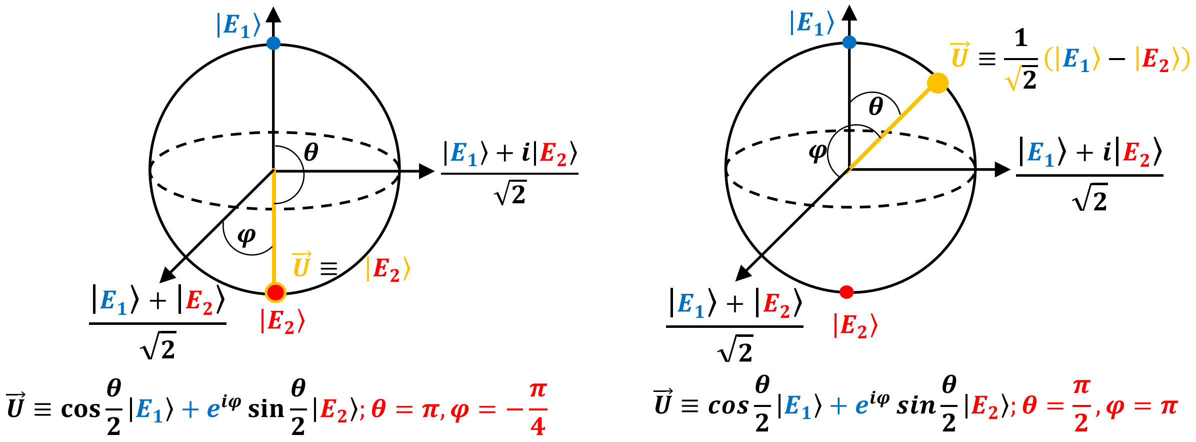

Figure 12: Classical analogue of Hadamard gate on Bloch sphere. The Hadamard gate 'rotates' the initial pure state of $|E_2\rangle$ **(a)** (also labeled (i) in Fig. 1d right panel) to a superposition of states **(b)** (also labeled (ii) in **Figure 11a** right panel) through a unitary transformation $\frac{1}{\sqrt{2}}\begin{pmatrix} 1 & 1 \\ 1 & -1 \end{pmatrix}$.

7. CONCLUSION

This research has comprehensively explored the intricate dynamics and novel phenomena inherent in quantum mechanics, highlighting significant potential as classical analogs to quantum mechanical behaviors through the classical nonlinear granular network. Through a meticulous combination of theoretical modeling, numerical simulations, and rigorous experimental validations, the research has elucidated how classical nonlinear granular networks can exhibit compelling quantum-inspired phenomena. Notably, this includes the emergence and manipulation of nonlinear normal modes (NNMs), the creation and evolution of state superpositions through elastic bits, and the realization of quantum-analogous computational gates.

Key contributions of this work include the innovative integration of elastic bits within classical elastic systems, specifically achieved through controlled manipulation via external driving forces. This research has delineated the fundamental distinctions between linearized and nonlinear granular systems: linearized systems permit external parameters to yield static, time-independent superposition states conducive to classical analog quantum logic gates, whereas nonlinear systems inherently produce rich, dynamic, time-dependent state superpositions. These observations offer crucial insights into the interplay between linearity and nonlinearity in the evolution of classical systems, illustrating how external control parameters—such as frequency, excitation amplitude, and system precompression—can profoundly influence dynamical behaviors without altering the intrinsic material properties.

Additionally, this research rigorously establishes the robustness, practicality, and tunability of nonlinear normal modes across diverse operational contexts. Systematic analysis across various damping levels, harmonic excitation conditions, and geometric configurations of granular networks has confirmed the reliability and adaptability of NNMs. Such findings bear critical implications for engineering applications, including advanced shock-mitigating materials, topologically robust acoustic waveguides, and quantum-inspired computational frameworks.

Looking forward, the study identifies several promising directions for future research. Notably, extending analytical frameworks to explore Berry phase phenomena within these classical systems represents a particularly exciting frontier. Manipulating the Berry phase through external excitations and temporal control of elastic bit parameters could deepen understanding of topological properties and bridge classical-quantum conceptual frameworks. Furthermore, the proposed development of a quantum-inspired mass sensor, leveraging the enhanced sensitivity arising from time-dependent superposition states, presents a promising practical innovation. This technology could potentially surpass conventional sensing mechanisms, such as Quartz Crystal

Microbalances and Bulk Acoustic Resonators, in terms of sensitivity and precision, and also provide novel insights into symmetry-breaking mechanisms analogous to those found in quantum mechanical models, like the Su–Schrieffer–Heeger (SSH) model.

Ultimately, this research underscores the profound potential of classical nonlinear granular systems as platforms for simulating and interpreting quantum mechanical phenomena. It not only opens novel frontiers in fundamental physics but also holds transformative promise for applied engineering and technological innovations.

REFERENCES

1. Arute, F., et al., *Quantum supremacy using a programmable superconducting processor.* Nature, 2019. **574**(7779): p. 505-510.
2. Deshpande, A., et al., *Quantum computational advantage via high-dimensional Gaussian boson sampling.* Science Advances, 2022. **8**(1): p. eabi7894.
3. Wu, Y., et al., *Strong Quantum Computational Advantage Using a Superconducting Quantum Processor.* Physical Review Letters, 2021. **127**(18): p. 180501.
4. Zhong, H.-S., et al., *Quantum computational advantage using photons.* Science, 2020. **370**(6523): p. 1460-1463.
5. Zhu, Q., et al., *Quantum computational advantage via 60-qubit 24-cycle random circuit sampling.* Science Bulletin, 2022. **67**(3): p. 240-245.
6. Silverman, M.P., *Quantum Superposition: Counterintuitive Consequences of Coherence, Entanglement, and Interference*. 2008: Springer Berlin Heidelberg.
7. Qiao, L.-F., et al., *Activation of entanglement from quantum coherence and superposition.* arXiv preprint arXiv:1710.04447, 2017.
8. Xi, Z., Y. Li, and H. Fan, *Quantum coherence and correlations in quantum system.* Scientific Reports, 2015. **5**(1): p. 10922.
9. LaPierre, R., *Introduction to Quantum Computing*. 2021: Springer International Publishing.
10. Nielsen, M.A. and I.L. Chuang, *Quantum Computation and Quantum Information: 10th Anniversary Edition*. 2010, Cambridge: Cambridge University Press.
11. Xu, X., et al., *Variational algorithms for linear algebra.* Science Bulletin, 2021. **66**(21): p. 2181-2188.

12. Guo, C., *Grover's algorithm–implementations and implications.* Highlights in Science, Engineering and Technology, 2023. **38**: p. 1071-1078.

13. Barkoutsos, P.K., et al., *Quantum algorithm for alchemical optimization in material design.* Chemical science, 2021. **12**(12): p. 4345-4352.

14. Vakili, M.G., et al., *Quantum computing-enhanced algorithm unveils novel inhibitors for KRAS.* arXiv preprint arXiv:2402.08210, 2024.

15. Hughes, C., et al., *Quantum Computing for the Quantum Curious*. 2021.

16. Montanaro, A., *Quantum algorithms: an overview.* npj Quantum Information, 2016. **2**(1): p. 15023.

17. Vakakis, A.F., *Analysis and identification of linear and nonlinear normal modes in vibrating systems*. 1991: California Institute of Technology.

18. Hasan, M.A. and P.A. Deymier, *Modeling and simulations of a nonlinear granular metamaterial: application to geometric phase-based mass sensing.* Modelling and Simulation in Materials Science and Engineering, 2022. **30**(7): p. 074002.

19. Narasimhachar, V. and G. Gour, *Low-temperature thermodynamics with quantum coherence.* Nature Communications, 2015. **6**(1): p. 7689.

20. Kato, K. *Quasi-Bell entangled coherent states and its quantum discrimination problem in the presence of thermal noise*. in *Quantum Communications and Quantum Imaging XIII*. 2015. SPIE.

21. Weber, P.E.R., et al., *Non-classical properties of superposition thermal quantum states.* Annals of Physics, 2022. **443**: p. 168986.

22. Ruostekoski, J., et al., *Macroscopic superpositions of Bose-Einstein condensates.* Physical Review A, 1998. **57**(1): p. 511-517.

23. Huang, Y.P. and M.G. Moore, *Creation, detection, and decoherence of macroscopic quantum superposition states in double-well Bose-Einstein condensates.* Physical Review A, 2006. **73**(2): p. 023606.

24. Brune, M., et al., *Observing the Progressive Decoherence of the ``Meter" in a Quantum Measurement.* Physical Review Letters, 1996. **77**(24): p. 4887-4890.

25. Deymier, P. and K. Runge, *Sound Topology, Duality, Coherence and Wave-Mixing: An Introduction to the Emerging New Science of Sound*. 2017.

26. Calderin, L., et al., *Experimental demonstration of coherent superpositions in an ultrasonic pseudospin.* Scientific Reports, 2019. **9**(1): p. 14156.

27. Sánchez Muñoz, C., et al., *Hybrid Systems for the Generation of Nonclassical Mechanical States via Quadratic Interactions.* Physical Review Letters, 2018. **121**(12): p. 123604.

28. Wood, B.D., S. Bose, and G.W. Morley, *Spin dynamical decoupling for generating macroscopic superpositions of a free-falling nanodiamond.* Physical Review A, 2022. **105**(1): p. 012824.

29. Freedman, M., et al., *Topological Quantum Computation.* Bull. Am. Math. Soc, 2001. **40**.

30. Alicea, J., et al., *Non-Abelian statistics and topological quantum information processing in 1D wire networks.* Nature Physics, 2011. **7**(5): p. 412-417.

31. Frolov, S., *Quantum computing's reproducibility crisis: Majorana fermions.* Nature, 2021. **592**(7854): p. 350-352.

32. Mahmood, K.T. and M.A. Hasan, *Topological insights from state manipulation in a classical elastic system.* AIP Advances, 2025. **15**(2).

33. Tan, H., et al., *Generation of macroscopic quantum superpositions of optomechanical oscillators by dissipation.* Physical Review A, 2013. **88**(2): p. 023817.

34. Brunelli, M. and O. Houhou, *Linear and quadratic reservoir engineering of non-Gaussian states.* Physical Review A, 2019. **100**(1): p. 013831.

35. Asjad, M. and D. Vitali, *Reservoir engineering of a mechanical resonator: generating a macroscopic superposition state and monitoring its decoherence.* Journal of Physics B: Atomic, Molecular and Optical Physics, 2014. **47**(4): p. 045502.

36. Abdi, M., et al., *Dissipative Optomechanical Preparation of Macroscopic Quantum Superposition States.* Physical Review Letters, 2016. **116**(23): p. 233604.

37. Buchmann, L.F., et al., *Macroscopic Tunneling of a Membrane in an Optomechanical Double-Well Potential.* Physical Review Letters, 2012. **108**(21): p. 210403.

38. Xu, H., et al., *Observation of optomechanical buckling transitions.* Nature Communications, 2017. **8**(1): p. 14481.

39. Ge, W. and M.S. Zubairy, *Macroscopic optomechanical superposition via periodic qubit flipping.* Physical Review A, 2015. **91**(1): p. 013842.

40. Gu, W.-j., et al., *Generation of non-classical states of mirror motion in the single-photon strong-coupling regime.* Optics Express, 2014. **22**(15): p. 18254-18267.

41. Pepper, B., et al., *Optomechanical Superpositions via Nested Interferometry.* Physical Review Letters, 2012. **109**(2): p. 023601.

42. Hoff, U.B., et al., *Measurement-Induced Macroscopic Superposition States in Cavity Optomechanics.* Physical Review Letters, 2016. **117**(14): p. 143601.

43. Montenegro, V., et al., *Macroscopic nonclassical-state preparation via postselection.* Physical Review A, 2017. **96**(5): p. 053851.

44. Liao, J.-Q. and L. Tian, *Macroscopic Quantum Superposition in Cavity Optomechanics.* Physical Review Letters, 2016. **116**(16): p. 163602.

45. Xiong, B., et al., *Generation of entangled Schrödinger cat state of two macroscopic mirrors.* Optics Express, 2019. **27**(9): p. 13547-13558.

46. Xie, H., et al., *Macroscopic superposition states of a mechanical oscillator in an optomechanical system with quadratic coupling.* Physical Review A, 2019. **100**(3): p. 033803.

47. Nesterenko, V.F., *Dynamics of Heterogeneous Materials*. 2001: Springer.

48. Mahmood, K.T. and M.A. Hasan, *Experimental demonstration of classical analogous time-dependent superposition of states.* Scientific Reports, 2022. **12**(1): p. 22580.

49. Coste, C. and B. Gilles, *On the validity of Hertz contact law for granular material acoustics.* The European Physical Journal B - Condensed Matter and Complex Systems, 1999. **7**: p. 155-168.

50. Jayaprakash, K.R., et al., *Nonlinear normal modes and band zones in granular chains with no pre-compression.* Nonlinear Dynamics, 2011. **63**(3): p. 359-385.

51. Vakakis, A.F., *Normal modes and localization in nonlinear systems.* 2001.

52. Starosvetsky, Y. and A.F. Vakakis, *Traveling waves and localized modes in one-dimensional homogeneous granular chains with no precompression.* Physical Review E, 2010. **82**(2): p. 026603.

53. Goldstein, H., C.P. Poole, and J.L. Safko, *Classical Mechanics*. 2002: Addison Wesley.

54. Lalov, I. and P. of Electromagnetic Phenomena, *The Physics of Vibrations and Waves: H.J. Pain, Wiley, New York, 1993 (Paper: ISBN 0-471-937428, Price US$ 29.95; Cloth: ISBN 0-471-936197, Price US$ 79.95). 479 pp.* Vibrational Spectroscopy, 1994. **6**(3): p. 379-380.

55. Goldstein, H., *Classical Mechanics*. 2011: Pearson.

56. Dür, W. and S. Heusler, *What we can learn about quantum physics from a single qubit.* arXiv preprint arXiv:1312.1463, 2013.

57. Lacarbonara, W., G. Rega, and A.H. Nayfeh, *Resonant non-linear normal modes. Part I: analytical treatment for structural one-dimensional systems.* International Journal of Non-Linear Mechanics, 2003. **38**(6): p. 851-872.

58. Lacarbonara, W. and G. Rega, *Resonant non-linear normal modes. Part II: activation/orthogonality conditions for shallow structural systems.* International Journal of Non-Linear Mechanics, 2003. **38**(6): p. 873-887.

59. Kerschen, G., et al., *Nonlinear normal modes, Part I: A useful framework for the structural dynamicist.* Mechanical Systems and Signal Processing, 2009. **23**(1): p. 170-194.

60. Oliveira, I., et al., *3. Fundamentals of Quantum Computation and Quantum Information*. 2007.

61. Williams, C.P., *Explorations in Quantum Computing*. 2010: Springer London.

ABSTRACT

NONLINEAR DYNAMICS-DRIVEN QUANTUM ANALOGUES IN CLASSICAL GRANULAR METAMATERIALS

by

KAZI TAHSIN MAHMOOD

May 2025

Advisor: Dr. M. Arif Hasan

Major: Mechanical Engineering

Degree: Master of Science

A fundamental concept of quantum mechanics that underpins quantum information processing is superposition. This study examines classical nonlinear systems, with a primary focus on two spherical granules influenced by external forces. It presents a method whereby gauge variants evolve naturally over time without modifying internal or external conditions. A perturbation-based model is developed to understand the nonlinear behavior of the granular model and its associated nonlinear normal modes. Our findings indicate a varied spectrum of vibrational modes affected by external driving forces and static precompression, which contrasts markedly with previous studies that identified only single resonances. Numerous distinct vibrational modes

are evident in highly nonlinear environments, whereas linear regimes exhibit singular mode behavior.

This research demonstrates the controlled manipulation of states in a two-level elastic bit, the classical counterpart of qubits, by manipulating coupled granules using external drivers. Employing a Bloch sphere representation, we experimentally implement quantum-analog logic gates and offer a comprehensive characterization of diverse system states, revealing insights into the nonlinear and topological dynamics of the system. External parameters are utilized to investigate transitions between various dynamical regimes, in contrast to conventional internal modification methods. Connecting classical and quantum dynamics via the manipulation of elastic system states enhances the applicability of topological concepts in material design and computational models.

Furthermore, we present experimental evidence for classical analogues of coherent superpositions of energy states facilitated by Hertz-type nonlinearities in granular systems subjected to external driving fields. Nonlinear vibrations manifest as linear modes, resulting in coherent superpositions that rely on their phase relationships. We experimentally demonstrate that the resulting amplitudes constitute state vectors that span a two-dimensional Hilbert space, allowing time to enable parametric exploration of this state space. This demonstration correlates the system's elastic properties with Bloch states, substantiating theoretical predictions via experimental validation. The superposition of classical states enables quantum-like computations without decoherence or wave function collapse. We experimentally demonstrate a reversible Hadamard-like operation, successfully producing classical superpositions.

This extensive study enhances our understanding of nonlinear granular systems, their capacity to replicate quantum phenomena, their potential applications in quantum-inspired computing, and the development of novel computational materials.

AUTOBIOGRAPHICAL STATEMENT

In the sphere of mechanical engineering at Wayne State University, my pursuit of a master's thesis titled “Nonlinear Dynamics-Driven Quantum Analogues in Classical Granular Metamaterials” represented a pivotal academic endeavor. I began a thorough study of granular networks, focusing primarily on the nonlinear dynamics of these networks while working with Professor M. Arif Hasan. Starting in the winter of 2022, I worked on the classical granular network to create a quantum-like structure that is superior to the conventional quantum bit. The formation of an elastic bit, analogous to the qubit in quantum mechanics, can be manipulated by applying external excitation. I have developed the necessary mathematical modulation of the superposition of states in both linearized and nonlinear networks. The linearized system can create superposed states that are time-independent and dependent on the change of the external excitation. The nonlinear network generates time-dependent superposed states that are not solely reliant on external excitation. These states also perform the quantum analogous logic gate operation, making it possible to create a data and information transformation process. These discoveries provide valuable guidance in the precise synthesis of quantum-based acoustic metamaterials. I extend profound gratitude to Professor M. Arif Hasan and the Acoustic Pseudospin and Topological Metamaterials Lab for their unwavering mentorship and support. This thesis signifies not only the culmination of an academic milestone but also the enduring spirit of inquiry that guides my trajectory forward.